INVESTIGATION OF ROOM TEMPERATURE SPUTTERING AND LASER ANNEALING OF CHALCOGEN RICH TMDs FOR OPTO-ELECTRONICS

Branden Spencer Gellerup

Thesis Prepared for the Degree of

MASTER OF SCIENCE

UNIVERSITY OF NORTH TEXAS

August 2022

APPROVED:

Andrey Voevodin, Chair
Nigel Shepherd, Committee Member
Christopher Muratore, Committee Member
Vijay Vasudevan, Chair of the Department of Materials Science and Engineering
Shengli Fu, Interim Dean of the College of Engineering
Victor Prybutok, Dean of the Toulouse Graduate School

Gellerup, Branden Spencer. *Investigation of Room Temperature Sputtering and Laser Annealing of Chalcogen Rich TMDs for Opto-Electronics*. Master of Science (Materials Science and Engineering), August 2022, 84 pp., 24 tables, 35 figures, 111 numbered references.

Chalcogen-rich transition-metal dichalcogenide (TMD) magnetron sputtering targets were custom manufactured via ball milling and sintering in the interest of depositing p-type chalcogen-rich films. Room temperature radio frequency (RF) magnetron sputtering produced ultra-thin amorphous precursor of WS_x and MoS_x (where x is between 2-3) on several different substrates. The influence of working pressure on the MoS_3 content of the amorphous films was explored with X-ray photoelectron spectroscopy (XPS), while the physical and chemical effects of sputtering were investigated for the WS_x target itself. The amorphous precursor films with higher chalcogenide content were chosen for laser annealing, and their subsequent laser annealing induced phase transformations were investigated for the synthesis of polycrystalline 2H-phase semiconducting thin films. The role of laser fluence and the number of laser pulses during annealing on phase transformation and film mobility was determined from Raman spectroscopy and Hall effect measurement, respectively. Hall effect measurements were used to identify carrier type and track mobility between amorphous precursors and crystalline films. The p-type 2H-TMD films demonstrates the ability to produce a scalable processing criterion for quality ultra-thin TMD films on various substrates and in a method which is also compatible for flexible, stretchable, transparent, and bendable substrates.

ACKNOWLEDGMENTS

First and foremost, my sincerest appreciation goes to Dr. Andrey Voevodin and Dr. Nigel Shepherd for allowing me to join their research group and conduct research under them for several years. This work would not be possible without our partners and my committee members Chris Muratore and Nick Glavin. My gratitude goes out to my peers and colleagues Corey Arnold, Euan Cairnes, Maddox Dockins, Renzo Sanchez, Shambhavi Raju Sakri, Christian Garcia, Jonathan Rodriguez, Khalil Omotosho, Oluwatosin Obe, and countless others for all their assistance and collaboration over the years. I also would not have been able to accomplish what I have without the work of my predecessors in the lab, such as Chukwudi Iheomamare, Benjamin Sirota, and Urmila Rathod. They laid the groundwork for my research during their graduate careers.

I appreciate the guidance of Dr. Rick Reidy, Dr. Samir Aouadi, and Dr. Thomas Scharff and their graciousness in allowing me the use of their facilities and acting as mentors through my undergraduate and graduate career at UNT. This research would not have materialized without aid from the MTSE lab supervisor Mr. David Garrett for training me on characterization techniques and always making sure all instruments are functional. I would like to acknowledge the MTSE administrators Ms. Lisa Dunlop and Ms. Tish Alexander for their unfettered support.

Finally, I would not be graduating without the unwavering support of my family, including my parents Mr. Erik Gellerup and Mrs. Pam Gellerup and my partner Ashton Lackie.

TABLE OF CONTENTS

Page

LIST OF TABLES

Page

LIST OF FIGURES

Page

CHAPTER 1

LITERATURE BACKGROUND

1.1 Motivations

The main objective of my research career is to contribute to the cost-efficiency ratio of photovoltaics. Making photovoltaics less expensive is also a goal of the Department of Energy (DOE), as in early 2021, the DOE announced an improvement in the 2030 target of solar cell cost-effectiveness: reducing the cost per kilowatt from the present-day cost of $0.046/kW to the intended 2030 price of $0.02/kW.[1] Apart from process engineering, improving upon the cost-effectiveness of solar cells are purely material issues.[2] One method to reduce the price of photovoltaics is by focusing on thin film materials with much lower manufacturing costs that can be produced in bulk. Low cost production methods could lower the capital costs of photovoltaics, which can be comparatively expensive.[3] Therefore, the goal of this work is to create a process to produce p-type TMDs, allowing the future creation of a P-N homojunction of TMDs to form thin film solar cells that are scalable and practically competitive to silicon (in which over 95% of cells are made of).[2]

1.2 2D Materials

After the discovery of graphene, an emergence of atomically flat two-dimensional (2D) materials such as transition metal dichalcogenides (TMDs), hexagonal boron nitride (h-BN), black phosphorous (BP), and transition metal carbides/nitrides (MXenes) have been sought out as potential candidates in sensors,[4-6] photodetectors, [7-8] transistors, [9-11] batteries, [12-14] and also in internet of things (IoT) devices.[4] This wide array of suitable applications owes to the unique combination of mechanical and electrical properties that may soon pave a road into

mainstream electronic applications as alternatives to conventional semiconductor materials (e.g. Si, GaAs, Ge, etc.). 2D semiconductors offer not only mono-to-few layer thicknesses, meaning low weight, flexibility, and the ability to fit into any application and on countless substrates, but also a high carrier mobility with large current on/off ratios.[15] Another benefit of being atomically thin is transparency. This coupled with ultra-high photo-responsivity, high light absorption, and efficient exciton production from photo-excitation seen in several 2D materials could make opto-electronics the first industry with widespread 2D usage alongside silicon.[4]

1.2.1 2D Devices Outlook

2D materials show potential as quick-response phototransistors, highly sensitivity photodetectors, self-powered solar cells, and as image sensors. [15-16] 2D materials have a competitive advantage over silicon (which holds most of the opto-electronics market) in high sensitivity and modulation frequency, but have struggled with low-frequency noise, large dark currents, and power consumption.[15] Thin film materials can be congruent with limiting the land usage of photovoltaics. The current solar panel farms are land intensive which adds to capital costs and also the operational cost from the leasing the land.[17] Adding solar cells to roofs is an indisputable method of harnessing solar power without the consequence of occupying more land area, and while the National Renewable Energy Laboratory (NREL) defines solar rooftop potential as the number of rooftops that can be retrofitted for solar power, only 26% of the surface area of roofs for residential buildings can be utilized for current bulk solar harvesters[18] where the remainder could be compatible with thin film photovoltaics.

1.2.2 Flexible/Stretchable Devices

2D materials could find its initial niche as dynamic devices that work in the field on

flexible substrates that conventional materials are too costly or cannot be used for. The demand for stretchable and conformal electronics is rapidly transforming the technology industry into the era of structural electronics. A primary cause is innovation in healthcare applications, medical treatments, and consumer products; which all require electronic devices to have intrinsic flexibility, optical properties, biocompatibility, and conformability to tissue surface.[19-20] For example, due to the necessity of photodetectors in daily operations, integration of photodetectors with flexible substrates allows a more widespread use of imaging, communications, manufacturing and transportation monitoring in applications previously inaccessible.[21] The demand for flexible electronics have allowed for the engineering of 2D TMD materials due to their exceptional mechanical, electrical, and optical properties.[9], [11], [19], [22-24]

1.2.3 Transition Metal Dichalcogenides

Transition metal dichalcogenides (TMDs) are a class of materials have been used in bulk form for over 50 years as solid lubricants and various applications,[25] but have only recently been used in their two-dimensional (2D) forms. These are layered compound semiconductors with strong-in-plane covalent bonds and weak Van der Waals forces out-of-plane.[26] Each layer contains a trigonal chalcogen atoms surrounded by metal atoms above and below and can form strain-free heterostructures due to van der Waals bonding at layer interfaces.[27] TMDs are sought out as potential candidates for electronic and optoelectronic devices such as batteries,[12-14] transistors [9-11], sensors,[5-6] photodetectors [7-8], [16], [28], and photovoltaics.[29]

1.2.4 MoS_2

Molybdenum disulfide (MoS_2) was first identified to form a 2H phase and discovered to the band gap shifted from indirect (1.3 eV) to direct (1.9 eV) at monolayer in 2010.[30] 2H-MoS_2

features high electrochemical activity as a strong catalyst with outstanding chemical stability.[31] MoS_2 is also inexpensive and is used in batteries,[13],[31] hydrogen evolution reaction (HER) fuel cells[31] and chemical sensing.[32] A semiconductor mono- and bi-layer 2H-MoS_2 can reach high mobilities >500 $cm^2 V^{-1} s^{-1}$ [27] and is used in field effect transistors (FETs),[11] photodetectors[28] and photovoltaics.[33-34] Oxidation concerns arise for applications in ambient environments,[13] or at increased temperatures where m-MoO_2 and α-MoO_3 are formed.[35]

1.2.5 WS_2

Tungsten disulfide, WS_2, is one of most widely used TMDs that exhibits an attractive combination of electrical and optical properties, such as in-plane carrier confinement and an ability to tune its band gap from an indirect band gap for bulk WS_2 (1.4eV) to a direct-bandgap when at a monolayer 2H-WS_2 (2.1eV).[36-38] These attributes as well as being abundant in nature and inexpensive[39-41] means that WS_2 is commonly employed in renewable energy applications such as in solar cells,[26], [37], [40], [42] in HER fuel cells[39], [43-45] and in rechargeable batteries.[12], [40], [42], [46] Tungsten disulfide shows promise in photovoltaic devices because of their tunable bandgap, high field mobility up to 50 $cm^2 V^{-1} s^{-1}$ and an on/off ratio above 10^5.[8]

1.3 TMD Manufacturing and Scalability

TMD films are generally fabricated by a top-down approach with chemical and mechanical exfoliation, or by a top-up approach from gaseous precursors in metal organic chemical vapor deposition (MOCVD) or atomic layer deposition (ALD),[24], [41], [47] However, these techniques offer low throughput and are not scalable, have a limited control over the growth size, or require harmful precursors.[24], [41], [46-47] CVD and exfoliated processing cannot be incorporated into very large-scale integration (VLSI).[24], [32], [41], [47] The expensive cost and

difficulty of fabricating heterostructures limits the advancement of MoS_2 films by CVD or exfoliation.[48]

Physical vapor deposition (PVD) methods such as magnetron sputtering offers an alternative route to provide low toxicity, high throughput, and large area processing of TMD films with uniform thickness that are reproducible on a wide-array of substrates with good adhesion.[11], [22], [24], [49] Utilizing room temperature magnetron sputtering allows for the deposition of ultra-thin TMDs onto polymeric substrates and do not require a transfer step for semiconducting device manufacturing that can introduce defects and is incompatible with wafer scale processes.[22], [49]

1.3.1 Laser Annealing of TMDs

While sputtering at room temperature does increase the S:W ratio, it leads to poor crystallinity and sub-stoichiometry,[36] where films produced by room temperature sputtering result in amorphous structures that do not have transport properties suited for desirable electronic and optoelectronic devices such as a decrease in mobility and increased carrier scattering.[9], [11], [19], [22], [23] Through the use of laser annealing, the amorphous TMD films with initially short-range atomic structuring can undergo a phase transformation into the hexagonal 2H phase P63/mmc. In this configuration the MX_2 films (where M is a transition metal and X are chalcogen atoms) form in a hexagonally packed 6-fold in-plane coordination structure.[38]

A certain threshold of laser energy is required for inducing reordering of transition metal and chalcogens from amorphous into the 2H phase. This energy threshold can be met by the absorption of laser irradiation which increases the highly localized temperature of the films.[50] Therefore, this process is wavelength dependent, and also depends on the laser

fluence, power density, rep rate, and number of pulses.[50] Since the temperature is the main factor towards crystallization, the laser interaction with the film and substrate and the thermal properties of both can affect the crystallization by conducting heat to or from the film.[19], [50], [51]

Laser annealing with excimer lasers such as KrF (248 nm) change the photon/material interactions due to a wavelength shift to the near-ultraviolet (UV) range of the light spectra. KrF lasers are pulsed rather than continuous, and the pulse width additionally affects the crystallization kinetics by changing the heating dynamics following the pulse energy delivery over the pulse width time.[11]

Magnetron sputtering routes for fabrication of amorphous ultra-thin TMD precursors have been used as a precursor for highly crystalline hexagonal TMDs achieved by the subsequent laser annealing.[9], [11], [19], [22], [23] The coupling of room temperature magnetron sputtering allows for the integration of 2D semiconducting TMDs into flexible electronics in a transfer-free processing method.[22] Recently, this coupling of laser annealing with room temperature magnetron sputtering has been demonstrated to promote crystallization of TMDs on PDMS substrates.[9], [11], [19], [23] This two-step synthesis technique commonly utilizes excimer lasers with short wavelength and a short pulse duration for annealing amorphous precursors on temperature limited substrates [52] and has enabled electronic MoS_2 devices to directly grown on PDMS substrates.[11], [28] The electron mobility of the MoS_2 channel was suggested to be limited by oxidation due to the existence of sulfur vacancies.[11]

1.3.2 Chalcogen-Deficient Sputtered TMD Films

A drawback of PVD growth of TMDs, including magnetron sputtering is that this processing method often leads to sub-stoichiometric films due to the high vapor pressure of the

chalcogen atoms, where chalcogens (such as sulfur) have three orders of magnitude higher vapor pressure than refractory metals, and the non-stoichiomtry of WS_2 is even worse than that of other TMDs due to a larger mass difference between the chalcogen and metal. [26], [49], [53], [54] Equal flux of TMD material is emitted from the sputtering target but a difference in mass causes sulfur to have a much lower mean free path, in addition sulfur can react with residual water in vacuum chamber, and less sulfur reaches the substrate, leading to sulfur deficient films.[26], [49] Increasing the deposition pressure, reducing growth temperature, and extending PVD growth for longer periods of time may partially compensate.[26], [36], [49], [54] However, the sticking coefficient of sulfur is less than that of the refractory metals, such as W, meaning that still sulfur will be inevitably lost on the substrates surface through desorption at a higher rate than W desorption rates and the resulting films S:W ratio will still be less than 2:1. [26], [49], [54] Using lower sputtering powers, deflecting energetic argon ion bombardment by additional external magnetic fields,[55] or setting a larger working distance between substrate and target produces less energetic bombardment of the sulfur atoms towards the substrate, resulting in a higher sulfur sticking factor.[26], [36], [49]

One result of PVD processing is that produced ultra-thin 2D TMD films are intrinsically n-type[44], [53] due to electron donating sulfur vacancies, V_s, and the proposed defect equation of WS_2 from Urmilaben P. Rathod et al. is as follows,

$$WS_2 \rightarrow S_2\,(g) + W_W^X + 2V_S^{\cdot\cdot} + 4e^- \quad (1)$$

where S_2 (g) is gaseous sulfur that is pumped away, W_W^X are neutral tungsten sites, and e^- are electrons.[54] As a result, changing sputtering parameters to adapt to all of the above methods that help to increase the S:W ratio will still result in a sub-stoichiometric film that is n-type if a

stoichiometric WS_2 target is used.[36]

1.4 Chalcogen-Rich TMDs

Manufacturing both p-type and n-type films is inherently required by the electronics industry for creating P/N junctions and heterojunctions for countless electronic and optical semiconductor applications.[53] Seeing as stoichiometric TMDs are natively n-type[44], [53], manufacturing p-type TMD films requires additional efforts. To create p-type semiconducting TMD films, ion implantation is typically used which requires complex equipment with potential safety hazards and limits the scalability of this technique. Thus, there is a need in PVD processing for making p-type TMD films with repeatable stoichiometry and in low-cost manner that conforms to long production runs and using closed low maintenance vacuum systems (e.g. production in-line systems with PVD chambers) that are typical of the semiconductor manufacturing process.[56] One method to achieve this is by adding other simultaneous chalcogen sources to magnetron sputtering in order to recoup the chalcogen loss, such as reactively sputtering with H_2S gas[49] or adding a PLD source of sulfur flux.[56] These additionally have drawbacks, such as needing to maintain another source while changing two different deposition techniques in-situ[56] , and also H_2S gas is toxic, corrosive, and flammable[57]

It has recently been reported that post-deposition annealing in sulfur precursors at an elevated temperature can be used to produce p-type TMD films.[36] The use of excess sulfur counteracts the effect of the sulfur vacancies and produce p-type films, by forming sulfur interstitial ions, S_i, according to a proposed equation from Urmilaben P. Rathod et al.,

$$\tfrac{1}{2}\, S_2 \leftrightarrow S_i^{j-} + jh \qquad (2)$$

where h are holes and j = 1 or 2.[36] However, the gaseous precursors used are dangerous, and

the >400 °C annealing temperature preclude a significant number of substrates, such as polymers, and this extra step often requires a break in the vacuum chamber which limits scalability and in general is not compatible for high throughput fabrication.[49]

TMD films themselves can produced chalcogen-rich rather than later introduced to more chalcogen content through annealing in a gaseous chalcogen overpressure. For example, both the W-S and Mo-S systems have the ability to form sulfur rich phases, where the phase diagrams for both systems can be found in Figures 1.1 and 1.2.[58-60].

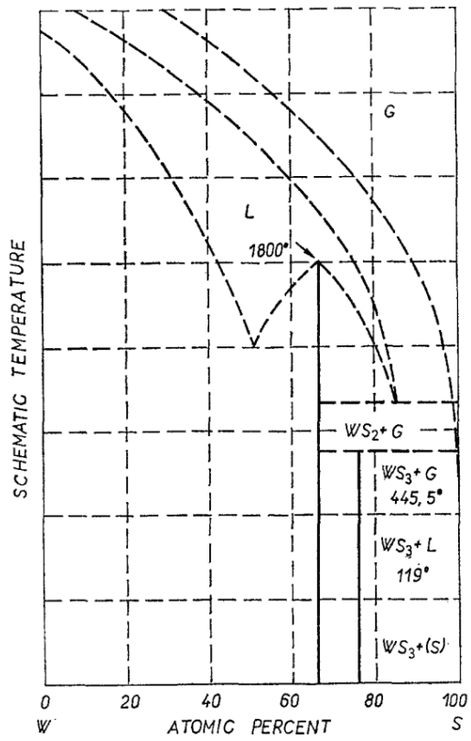

Figure 1.1: Phase diagram of the W-S system.[58]

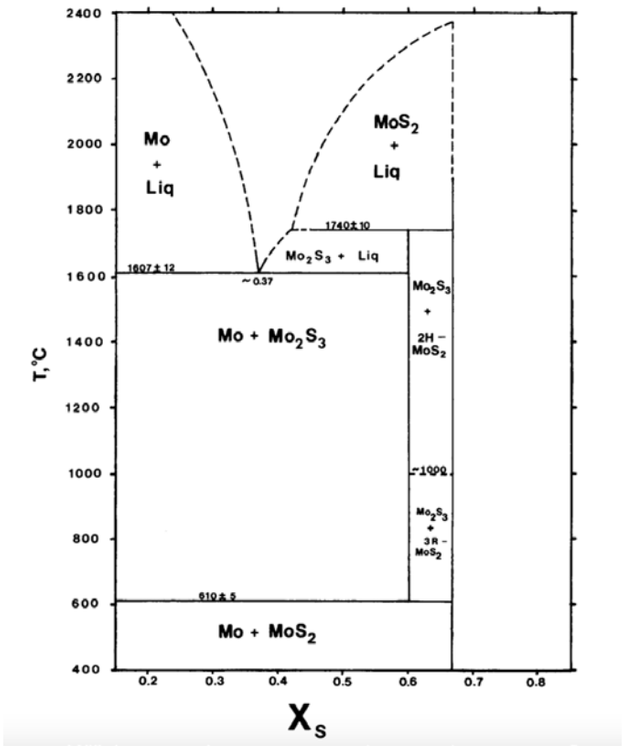

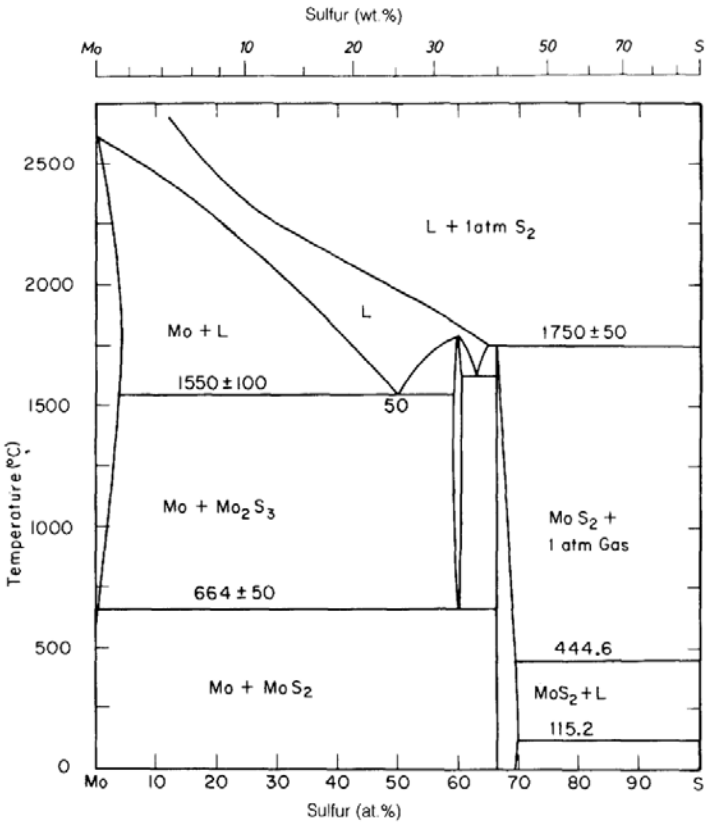

Figure 1.2: Phase diagrams of Mo-S system.[59-60]

WS_3, and MoS_3, and WSe_3 compounds have been researched since the 1970's [68] and are unusual as they have been experimentally synthesized, but only in the amorphous form.[61-63] A proposed reaction for MoS_3 formation,

$$MoS_2\,(s) + S_2\,(s) \rightarrow Mo^{5+}[(S_2)^{2-}]_{1/2}(S^{2-})_2\,(s) \qquad (3)$$

where the molybdenum atoms are interchangeably linked by the bridging sulfur and disulfide ion which is similar to the structure of crystalline NbS_3 [64-68]. However, this structure and many others are still debated. It is widely held that MoS_3 forms either chain-like or cyclic models in either a 1D or 2D nanostructure,[66], [68] such as linear chains of that share edges and faces of prisms,[69-70] or trigonal building blocks.[68] However, recently density function theory (DFT) calculations ruled out strictly linear models due and if a chain-like structure did exist it would be

curved due to S_2 dimers in open-rings, rings, wave-like, or helical structures.[68]

1.4.1 Amorphous Sulfur-Rich TMD Synthesis Techniques

MoS_3 and WS_3 are untapped resources that are waste product formed in the purification of MoS_2 and WS_2.[71] Otherwise, amorphous sulfur-rich TMDs can be synthesized using conventional TMD fabrication techniques[41], [45] but are more commonly produced via electrochemical and electrodeposition techniques with acids,[*63*], [66], [69], [72-76] or the thermal decomposition of ammonium tetrathiotungstate or tetrathiomolybdate.[46], [57], [66-67], [69], [77-78] These approaches require a large quantity of precursors such as metal organics and H_2S or reagents with H_2S intermediates are both environmentally damaging[31], [41] and dangerous to use.[57] As such a PVD based process is necessary, where solid earth abundant powder is used to produce the sources.

1.4.2 Amorphous Sulfur-Rich TMD Applications

Amorphous MoS_3 and WS_3 are used for electrocatalytic activities where their amorphous structure exposes more active sites than crystalline samples. Electrochemical applications include hydrogen evolution reaction (HER) and N_2 fuel cells,[45], [*57*], [69], [73-74], [79-80], [85] electrodes in batteries,[61], [63], [66-67], [75], [80-86] catalytic tribological coatings,[62], [76]constituents in organic photovoltaic cells and gas capture systems.[72] They are also often used as precursors or intermediates to form oxides or different compounds.[68], [76-77]

1.4.3 Chalcogen-Rich Sputtering Targets

A way to directly integrate the excess-sulfur required to form p-type TMDs, which is inexpensive and does not necessitate another manufacturing step nor the use of a synchronous

sulfur source, is by making the sputtering target itself a sulfur-rich source by making it over-stoichiometric. Sulfur is environmentally friendly, inexpensive, and nontoxic[87-89] and serves the added benefit of acting as a binder for TMD materials.[53] Starting from this composition with an abundance of sulfur lowers the margin of error from the higher vapor pressure and substrate desorption, and sulfur loss still results in an overstoichiometric TMD film rather than a substoichiometric film produced by a stoichiometric target.

These targets are advantageous for sputtering p-type films and have the potential to be tailored for to the individual need of the sputtering user for specific compounds, stoichiometry, or doping concentration to tune n- or p-type conductivity and electrical behavior,[53] where that level of control has been shown for electrodepositing TMDs by varying the amount of sulfur precursor.[74]

TMD sputtering targets are commonly made by spark plasma sintering,[90-93] where metal sulfides and selenides are made to great success for use sputtering thermoelectric material such as SnSe,[94] SnS_2,[95] VSe_2,[96] and Sb_2Se_3.[29] Sintered products can be fabricated at a much lower temperature and higher purities and finer microstructures which can provide superior sputtering performances.[97] The use of short heating times and using a graphite die was found to suppress sulfur loss while preventing the oxidation of metal sulfides during heating.[98] Chalcogen-rich sputtering have also been prepared by spark plasma sintering (SPS), such as $NiSe_2$ with extra selenium powder and NiS_2 with excess-sulfur powder placed into a die for 10 min at 600°C.[99] Still little is known in terms of such targets behavior during sputtering to assess stability of the target performance over extended runs suitable for TMD film growth in device manufacturing.

1.5 Knowledge Gaps

The literature review above has identified several knowledge gaps in the processing of excess-chalcogen films and sputtering targets needed for their production.

1.5.1 Chalcogen-Rich Target Manufacturing

At the time of writing, only two chalcogen-rich TMD sputtering targets have previously been reported in literature, all by SPS instead of traditional manufacturing. Most amorphous MoS_3 and WS_3 sources are gaseous or liquid, so it is not known how chalcogen-rich powders would differ from traditional solid-state sintering or liquid phase sintering.

1.5.2 Chalcogen-Rich Target Sputtering

Little is known of the sputtering stability, behavior, and performance of chalcogen-rich targets, especially for those not manufactured via SPS. Investigation is lacking into how electrical biasing and plasma interactions effect the targets and subsequently the resulting sputtered films.

1.5.3 Sputtering and Laser Annealing Sulfur-Rich Precursors

Depositing films from excess-chalcogen targets has not been reported as of the time of writing. It is unknown if this process can yield p-type semiconducting TMD films. Additionally, it is not clear if the deposition process can be successful at room temperature. For the amorphous precursors subsequent laser annealing, the crystallization threshold for amorphous sulfur-rich films also needs to be determined. Further, it is not known if the crystallization threshold of the amorphous sulfur-rich films dependent on the thermal properties of the substrate used similarly as to stoichiometric films.

1.6 Scientific Hypothesis and Research Objectives

Hypothesis: P-type semiconducting films can be produced from laser annealing of chalcogen-rich precursors deposited from excess-chalcogen targets with high S:W ratio

The following objectives of this thesis are guided the testing of aforementioned hypothesis:

1. Chalcogen-rich target manufacturing
    a. Compare the targets made by hot pressing and vacuum sintering
    b. Study the surface morphology of the sintered targets
2. Chalcogen-rich target sputtering
    a. Determine the mechanism for the change in S:W ratio and oxidation of a sputtering target over its use and how excess sulfur effects it
    b. Confirm if this mechanism effects stoichiometric targets
3. Sputtering and laser annealing sulfur-rich precursors
    a. Deposit a sulfur-rich film through the sputtering of an excess-sulfur target
    b. Laser anneal the sulfur-rich MoS_2 precursors into p-type 2H-MoS2
    c. Crystallize 2H-MoS2 onto various substrates

CHAPTER 2

METHODS

2.1 Sputtering Target Preparations

2.1.1 Materials

Chalcogen-excess (chalcogen to transition metal ratio > 5) powder was prepared from MoS_2 and sulfur, WS_2 and sulfur, and WSe_2 and selenium powder (sourced from Aldrich Chemistry, 99% and 99.98% purity, respectively) which was ground into a homogenous mixture in a mortar and pestle under a fume hood or a glovebox filled with a N_2 overpressure and either ball-milled or acoustically mixed with steel medium for 24 hours and five minutes, respectively. A Plasmaterials stoichiometric WS_2 target of 99% purity was additionally sputtered for comparison purposes.

2.1.2 Hotpressing

The powder was poured into a 1.3-inch diameter steel packing die which was used to prepare green pellets and to sinter sputtering targets. Targets were prepared by hotpressing with a Carver hydraulic press at 75°C at 15,000 lbs for three days.

2.1.3 Liquid Phase Sintering

The powder mixed in a glovebox and with a labRAM acoustic mixer was pressed into a green pellet using the 1.3-inch diameter die and liquid phase sintered in a vacuum furnace. The sintering either used the packing die as a vessel or the green pellet was ejected and placed onto an alumina boat. Titanium foam was placed into a tungsten crucible which was placed near the target and used as a getter for oxygen.

The tube furnace was allowed to heat up to 300°C and pump down with a roughing pump for 24 hours while 5 sccm of argon gas was run into the furnace. After that 24 hour period the target was liquid phase sintered in the vacuum furnace at 300°C for 24 hrs.

2.2 TMD Thin Film Synthesis

2.2.1 Magnetron Sputtering

A box chamber with two magnetron sputtering guns was used to produce the amorphous chalcogen-rich precursors.

Figure 2.1: **Sputtering box chamber (left) with magnetron sputtering in use (right).**

The chamber is loaded with targets and substrates (such as polymers, silicon, glass, etc.) The door to the chamber was then closed, and an attached roughing pump was used to pump the chamber down to 1 mTorr before the attached turbopump was activated. Depositions began when the turbo pumped vacuum chamber reached 10^{-7} Torr base pressure or lower. The sputtering targets on the magnetron guns both had pulse direct current (DC) and radiofrequency (RF) power supplies, where an RF power supply was required to start a plasma

for the chalcogen-rich targets. The sputtering targets were presputtered for typically three minutes or longer behind a shutter while water-cooled through the entire process.

2.2.2 WS_x and MoS_x Film Growth

For depositing excess-sulfur precursors, such as WS_x and MoS_x, a sputtering power density of 18.18 W/cm^2 was used at room temperature. Argon gas was introduced at a 25 sccm flowrate with a working pressure to start the plasma which was then reduced to either 10 or 20 mTorr. The samples were at a working distance of 2.5 cm and were on a stage that rotated to allow a higher throughput of sputtered precursor.

2.2.3 BON Film Growth

A plasmaterials boron nitride (BN) target of 99.5% purity was used to deposit the amorphous boron-oxynitride (BON) which was used as a dielectric and encapsulant for the TMDs. A sputtering power density of 26.26 W/cm^2 was used at room temperature. Nitrogen gas was introduced at a 20 sccm flowrate with a working pressure of 85 mTorr which was used to start the plasma and reduced to either 5 or 15 mTorr.

2.3 Laser Annealing of Thin Films

Following the TMD amorphous precursor film growth, a 248 nm Lambda Physik Novatube KrF laser with an unfocused beam footprint of 1 x 3 cm was used for laser annealing to crystalize as-deposited MoS_x to 2H-MoS_2 thin films at room temperature and atmospheric pressure. The films were annealed at laser beam energies between 100-450mJ at 1 Hz pulse frequency for 1, 5, and 10 pulses. The maximum fluence of the system is 450 mJ directly after a gas refill.

2.4 Material Characterization Methods

2.4.1 Profilometry

The thickness of deposited films were determined by a Veeco Dektak 150 stylus profilometer, where a step was created on the film by way of a glass cover slip or heat resistant on the substrate for depositing the film. The stylus of the profilometer runs along the substrate and is deflected by the step, which is used to determine the thickness and growth rate of a sample.

2.4.2 Scanning Electron Microscopy

Both films and sputtering targets were characterized with a Hitachi TM300 scanning electron microscope (SEM) with energy dispersive spectroscopy (EDX) capabilities. SEM images were taken in backscattered electron (BSE) modes for information on chemical distribution of samples and secondary electron (SE) mode for surface morphological information. EDX maps were created by collecting W Mα1, Mo Lα1, Se Lα, and S Kα1, and O Kα1 characteristic X-rays.

2.4.3 Raman Spectroscopy

A Renishaw Virsa Raman analyzer with a 532 nm laser was used to confirm the amorphous nature of the films deposited at room temperature and determine the crystalline nature of the films after laser annealing. Information on the samples structure and identification of different species can be determined by characteristic vibrational modes from Stokes shifts. The system used for this work was not able to detect low-Stokes to anti-Stokes photon shifts due to a noise filter on the CCD detector. Laser powers less than 10% were used in order to prevent unintended damage or changes in crystallinity. A silicon wafer was used to calibrate the system between each use.

The relationship between the two characteristic 2H-WS_2 vibrational modes $E^1_{2g}(\Gamma)$ (in-pane vibration) and $A_{1g}(\Gamma)$ (out-of-plane vibration) have been reported extensively.[24], [37-38] The broadening of the E′ line is generally recognized to be caused by overlap from a double 2LA(M) process, where the LA(M) motion is in-plane collective lattice movement.[37], [100] These peaks must be separated via deconvolution in order to assign both peaks within the E′ line, and even the assignment still could be arbitrary. Yet, the $E^1_{2g}(\Gamma)$ and 2LA(M) modes seem to be used synonymously in papers that do not deconvolute their peaks within the E′ line. For example, Qiao et al. report their $E^1_{2g}(\Gamma)$ peaks between 348-352 cm^{-1} while Berkdemir reports peaks within this same range as the 2LA(M) mode while reporting $E^1_{2g}(\Gamma)$ from 354-355 cm^{-1} for all samples and thicknesses.[37-38] Additionally, either of the two vibrational modes could be of higher intensity, as 2LA(M) mode has been reported as being roughly twice the relative intensity as the $A_{1g}(\Gamma)$ mode due to a double resonant process.[37-38] These inconsistencies make the deconvolution and assignment of the overlapped vibrational modes within the E′ line dubious, which is why deconvolution of the peaks for this work was avoided and assignment was based on peak location alone for the most intense point within the E′ line. Additionally, using peak intensity ratios should be approached with caution as either $E^1_{2g}(\Gamma)$ or 2LAM can be more intense and the overall position of the E′ line can shift due to various factors (thickness, stress/strain, etc.) and it is unclear if peak intensity ratios of $E^1_{2g}(\Gamma)$:$A_{1g}(\Gamma)$ and 2LAM:$A_{1g}(\Gamma)$ are interchangeable for correlating to film properties.

2.4.4 X-Ray Photoelectron Spectroscopy

Chemical composition of the MoS_x films was analyzed with a PHI 5000 Versaprobe

Scanning X-ray photoelectron spectroscopy (XPS) with monochromatic 1,486.6 eV Al Kα radiation. High-resolution Mo 3d, S 2p, O 1s, and C 1s XPS spectra were collected over the binding energy range of 0 to 1100 eV. Peak positions were calibrated for all scans using the C 1s peak with a binding energy of 284.80 eV. The Gaussian-Lorentzian function with a 30% Lorentz contribution, GL (30), was used to deconvolute the high-resolution peaks with a Shirley or linear background subtraction.

2.4.5 Hall-Effect Measurements

An Ecopia HMS5000 Hall measurement system with the Van der Pauw contact configuration was used for electrical measurements. Indium (In) metal (workfunction 4.1 eV) was used for contacts as it readily forms ohmic contacts. Electrically insulating substrates are required for use. Semiconducting properties such as carrier type, carrier density, and mobility were recorded. The amorphous TMDs were found to be too resistive for measurements and crystallization was required before analysis

2.4.6 X-Ray Diffraction

The crystal structure of the targets was investigated using a Rigaku Ultima III X-ray diffractometer at a scan speed of 3 deg/min with 40kV Cu Kα incident beam in a coupled 2theta/omega scan axis. The X-ray diffraction (XRD) data was analyzed using JADE software by selecting the diffraction peaks and calculating interatomic spacing, full width at half maximum (FWHM), and crystallite size.

CHAPTER 3

RESULTS AND DISCUSSION

3.1 Manufactured Chalcogen-Rich Targets for Magnetron Sputtering of TMD Films

Excess-chalcogen WS_{2+}, MoS_{2+}, and WSe_{2+} sputtering targets were manufactured with various manufacturing techniques described in Section 2.1 and were compared based on resulting target morphology and chemical composition.

3.1.1 WS_{2+} Targets

A $WS_{2.7}$ target was prepared from ball-milling and hotpressing as confirmed by EDX, but had a large amount of oxygen inclusions, shown in Table 3.1, due to both the 24 hours of ball milling and the three days of sintering both being done in an ambient environment.

Table 3.1: EDX compositional data of $WS_{2.7}$ target made from ball milling and hotpressing.

Element	Atomic %
S	60.17
W	23.2
O	16.63
Total	100

The $WS_{2.7}$ powder was likely supersaturated with sulfur, which precipitated out into a separate sulfur phase as shown in EDX mapping in Figure 3.1, and a pattern resembling a spinodal phase can be seen on the unsputtered $WS_{2.7}$ target in Figure 3.2.

The decomposition of the unsputtered $WS_{2.7}$ target is likely due to the instability of the WS_3 compound, and could be indicative of the WS_3 + S phase.[58] Tan et al. also reports a sample of similar composition, $WS_{2.64}$, that was initially WS_3 and underwent a partial conversion to WS_2, with a proposed chain-like structure of S^{2-} and S_2^{2-} ligands.[41]

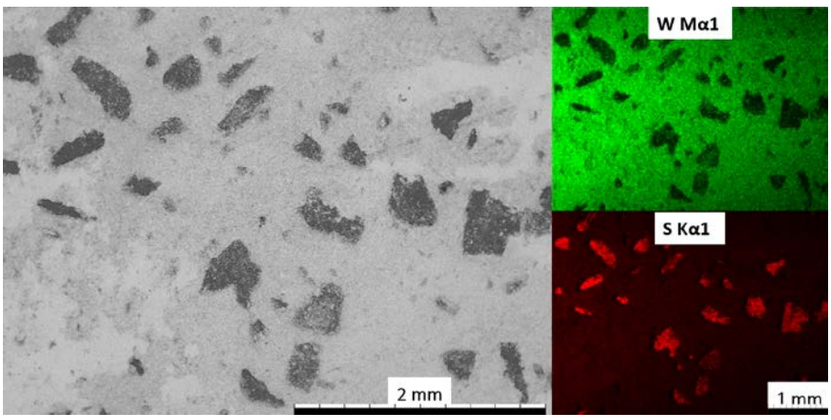

Figure 3.1: **SEM image and EDX scans of unsputtered $WS_{2.7}$ target that was manufactured from ball milling and hotpressing.**

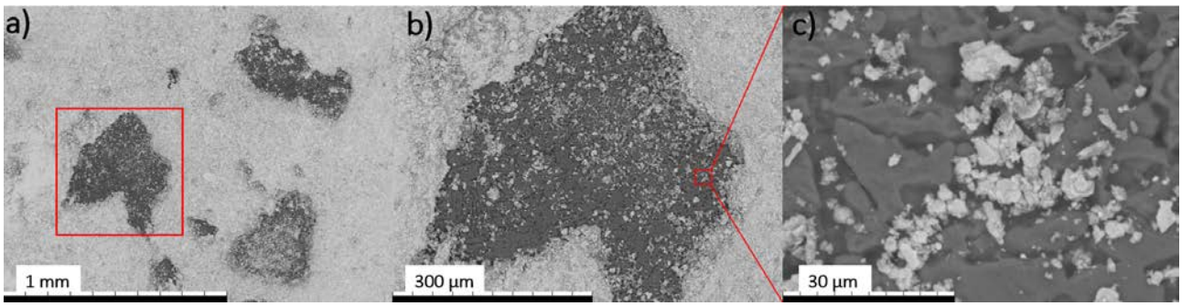

Figure 3.2: **SEM images of unsputtered $WS_{2.7}$ target, a) BSE x100, b) BSE x300, c) BSE x2500 magnification.**

In an effort to decrease the oxidation of the target, the target powder was mixed in a glovebox with a nitrogen overpressure, then the powder was placed into an acoustic mixer for 5 minutes, and finally hotpressed. This process significantly reduced the sulfur precipitates in the target and increased the homogeneity as seen in Figure 3.3, which is likely due to a more thoroughly mixed powder.

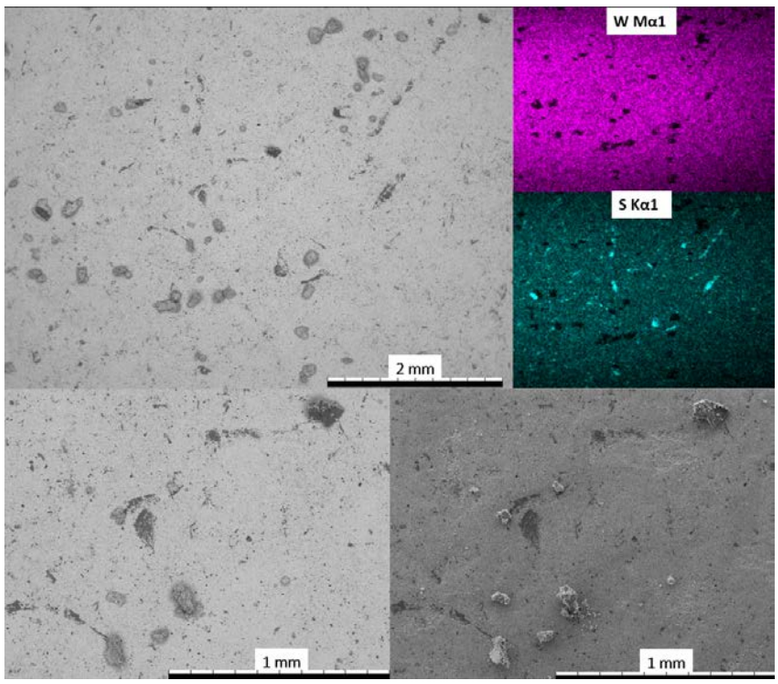

Figure 3.3: **SEM images and EDX scans of unsputtered $WS_{2.4}$ target that was manufactured from a combo of glovebox/acoustic powder mixing and hotpressing.**

However, the porosity of the target increased. The target produced by the glovebox, acoustic mixing, and hotpressing process had a slightly lower S:W ratio of 2.4:1 and had an increase of oxygen, as found in Table 3.2. This could similarly be a result of a more thorough mixing of the mix as the acoustic mixing is done in an ambient atmosphere and seems to introduce more oxygen in 5 minutes than ball milling does in 24 hours.

Table 3.2: EDX compositional data of $WS_{2.4}$ target made from ball milling and hotpressing.

Element	Atomic %
O	18.2
S	56.7
W	25
Total	100

To find a target processing method that does lower the oxygen liquid-phase sintering was utilized in a vacuum chamber. Resultingly a $WS_{2.3}$ target was manufactured, and a marked reduction in oxygen occurred; less than half of that for the $WS_{2.4}$ and $WS_{2.7}$ hotpressed targets, as shown in Table 3.3.

Table 3.3: EDX compositional data of $WS_{2.3}$ target made from liquid phase sintering.

Element	Atomic %
S	64.71
W	28.43
O	6.86
Total	100

The targets are more homogenous than the $WS_{2.4}$ hotpressed target made from acoustic mixing of the target powder, with no separate sulfur phases formed as shown in the EDX mapping in Figure 3.4. However, a noticeable increase in porosity occurred likely due to the lack of pressure on the target during sintering.

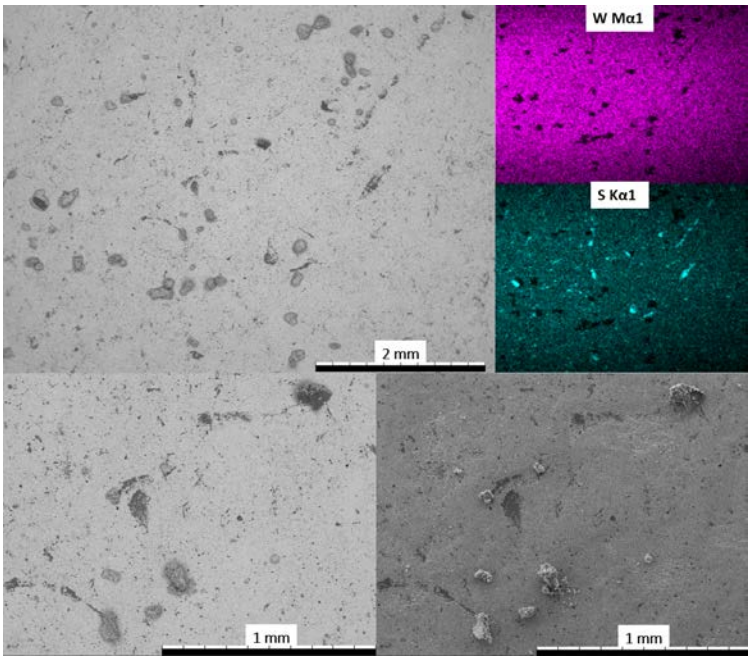

Figure 3.4: **SEM images and EDX scans of unsputtered $WS_{2.3}$ target which was manufactured from liquid phase sintering in a vacuum furnace.**

To additionally compare the manufacturing methods of the three aforementioned WS_{2+} targets, the crystallinity of the of targets were investigated with XRD where the results are presented in Figure 3.5.

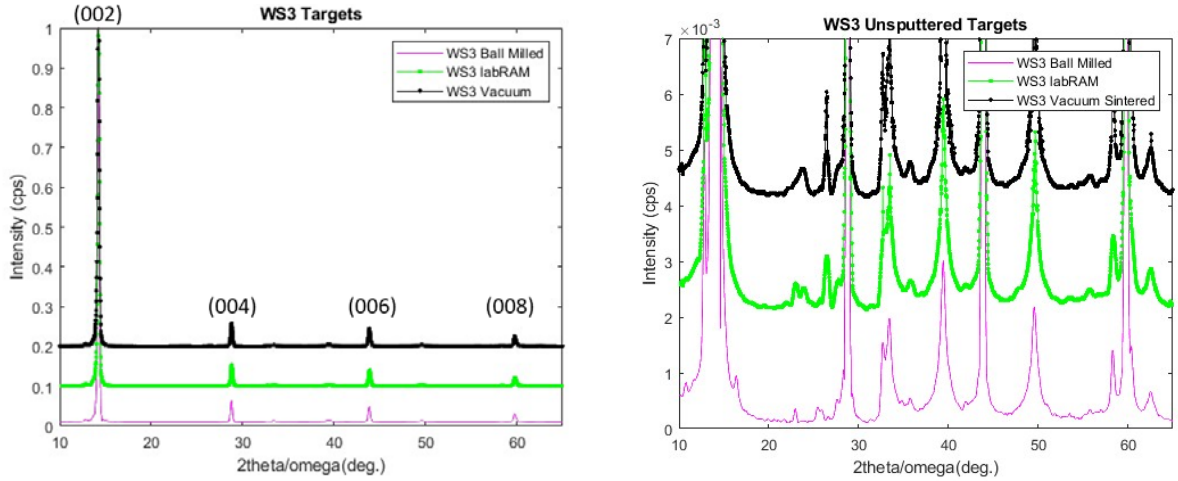

Figure 3.5: **Diffraction spectra from coupled 2theta/omega XRD scans of the manufactured WS_{2+} sputtering targets.**

All three targets are highly crystalline and all displayed a dominant (002) hkl peak of

hexagonal WS_2 phase, and shared all bulk poly-crystalline diffraction peaks with the original WS_2 powder and other XRD patterns from literature.[39], [44] All targets were highly textured in the (002), (004), (006), and (008) orientations. No discernable difference can be found from the high-resolution spectra in Figure 3.5, meaning the found porosity and morphology differences had no significant effect on the targets crystallinity or texture.

3.1.2 WSe_{2+} Targets

A $WSe_{4.2}$ target was manufactured by ball milling and hotpressing which yielded the highest chalcogen:transition metal ratio among targets investigated in this work, much higher than that of the sulfur based targets. Additionally, it had a fairly low relative percentage of oxygen as shown in Table 3.4.

Table 3.4: EDX compositional data of WSe_{2+} target made by hotpressing.

Element	Atomic %
Se	72.42
W	17.31
S	2.55
O	7.72
Total	100

Liquid phase sintering was attempted to increase the Se:W ratio and reduce the oxygen content further, but it did not accomplish either, and actually drastically reduced the Se:W ratio while increasing the oxygen content drastically, according to EDX results in Table 3.5.

Table 3.5: EDX compositional data of WSe_{2+} target made from liquid phase sintering.

Element	Atomic %
Se	27
W	20.3
O	52.7
Total	100

The chalcogen:transition metal ratio of the $WSe_{1.3}$ target was the lowest of all targets produced in this work. Selenium seemed to have melted from the target while resting on the alumina boat during sintering and left residue on the boat. The loss of selenium was replaced nearly 1:1 with oxygen. The morphology of the targets was compared in Figure 3.6, where the liquid phase sintered target was more homogenous than the hotpressed target, while being much more porous due to the loss of the selenium.

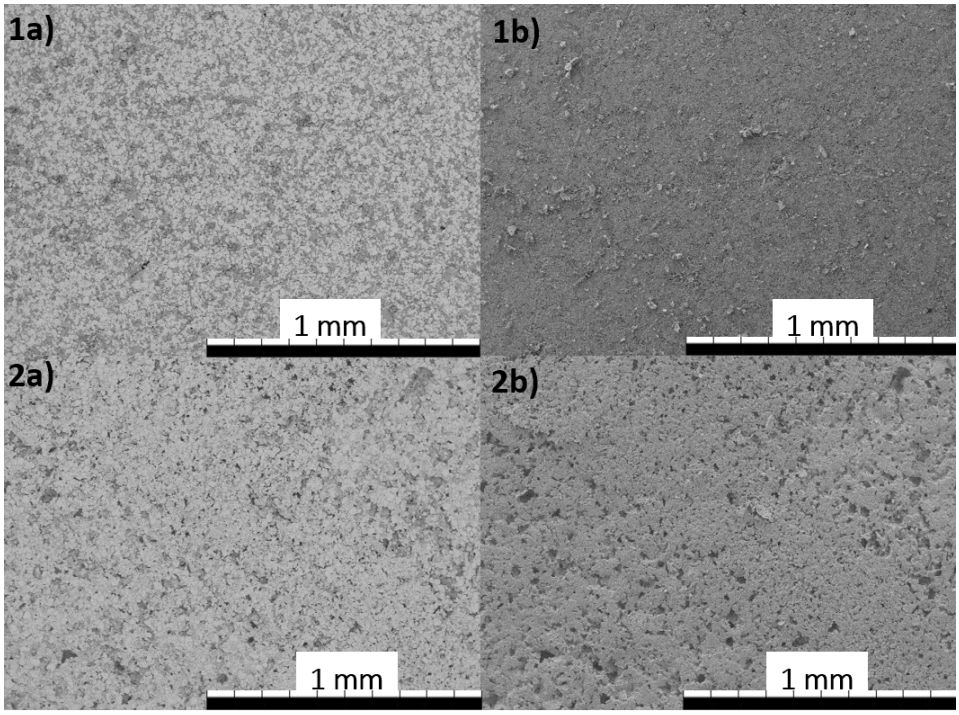

Figure 3.6: SEM images of unsputtered $WS_{4.2}$ target produced by hotpressing (1a-b), and the unsputtered $WS_{1.3}$ target produced from liquid phase sintering (2a-b).

3.1.3 MoS_{2+} Targets

A MoS_{2+} target was produced from ball milling and hotpressing, resulting in a S:Mo ratio of 2.09 but a considerable amount of oxygen was also present according to EDX results in Table 3.6. The presence of tungsten in the target is due to reuse of a steel packing dye, mortar and pestle, and mixing containers.

Table 3.6: EDX compositional data of the unsputtered MoS_{2+} target.

Element	Atomic %
S	51.04
Mo	24.47
W	1.59
O	22.9
Total	100

Following sputtering the target for 33 minutes the target has a new S:Mo ratio of 1.88:1 and the oxygen content was reduced, according to EDX scan results in Table 3.7.

Table 3.7: EDX compositional data of the MoS_{2+} target after 33 mins of sputtering.

Element	Atomic %
S	54.81
Mo	29.1
W	1.69
O	14.4
Total	100

The MoS_{2+} target was then polished and experienced an increase in S:Mo ratio to 3.61:1 and another gradual decrease in oxygen content according to Table 3.8.

Table 3.8: EDX compositional data of the MoS_{2+} target after 33 mins of sputtering.

Element	Atomic %
S	68.28
Mo	18.91
W	1.89
O	10.92
Total	100

The morphology change as a function of sputtering time was investigated via SEM images which are show in Figure 3.7. An explanation as to why the oxygen content trends down after sputtering use and polishing is there was likely an oxide on the surface of the initial

unsputtered target that formed during sintering, which is removed by sputtering and polishing. As a result of this removal of the oxide, the S:Mo ratio of 3.6:1 of the bulk target volume is measured after polishing the surface.

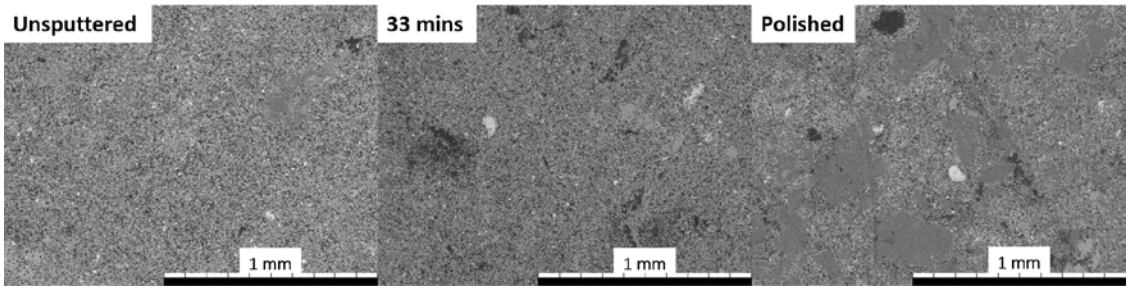

Figure 3.7: **SEM images of unsputtered $MoS_{3.6}$ sputtering target after sputtering and polishing.**

3.2 W-S Based Target Sputtering

The unsputtered $WS_{2.7}$ target that was produced by ball-milling and sintering was characterized after the total sputtering time reached three minutes, 36 minutes, 96 minutes, and five hours. A pulse DC power supply was not sufficient to strike a plasma on the $WS_{2.7}$ target, and, hence, a RF power supply was required to start the plasma since sulfur is electrically insulating.[102]

3.2.1 Chemical Composition and Morphology

A typical erosion groove produced during planar magnetron sputtering from the non-uniform plasma distribution was formed on the commercial stoichiometric target after a total sputtering time of 10 hours with a 1mm width as shown in Figures 3.8 and 3.9. This is typical overall behavior well known to sputtering community practitioners.

In contrast, the overstoichiometric $WS_{2.7}$ target did not exhibit such erosion groove formation even after a total sputtering time of 10 hours occurred. Despite the absence of the sputtering groove on the surface of the sulfur-rich target, it had shown a clear evolution of the

composition over the sputtering time. Figure 3.10 shows the tracking of chemical composition of the $WS_{2.7}$ target over the extended sputtering time investigated via EDX mapping of target surface at random locations and averaged for the target's surface.

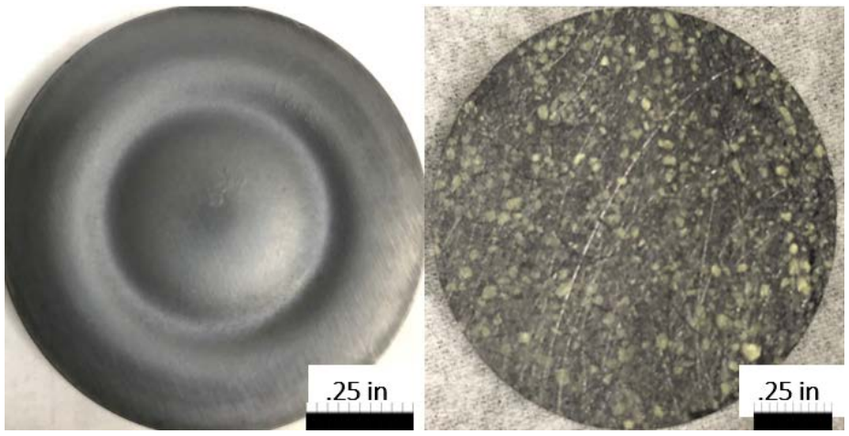

Figure 3.8: **Picture of erosion groove that forms on sputtering targets as a result of magnetron sputtering vs the lack of erosion groove of sulfur-rich target.**

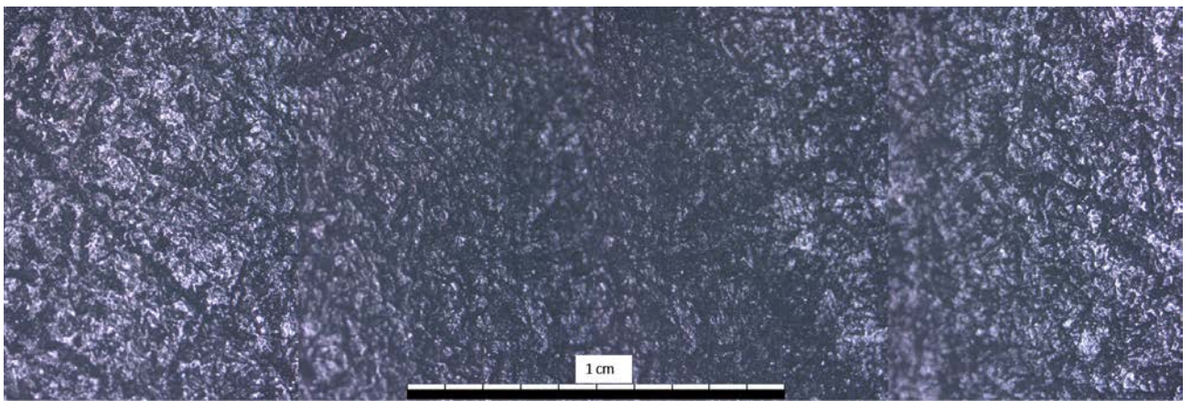

Figure 3.9: **Optical image of the erosion groove of the sputtered commercial WS_2 target.**

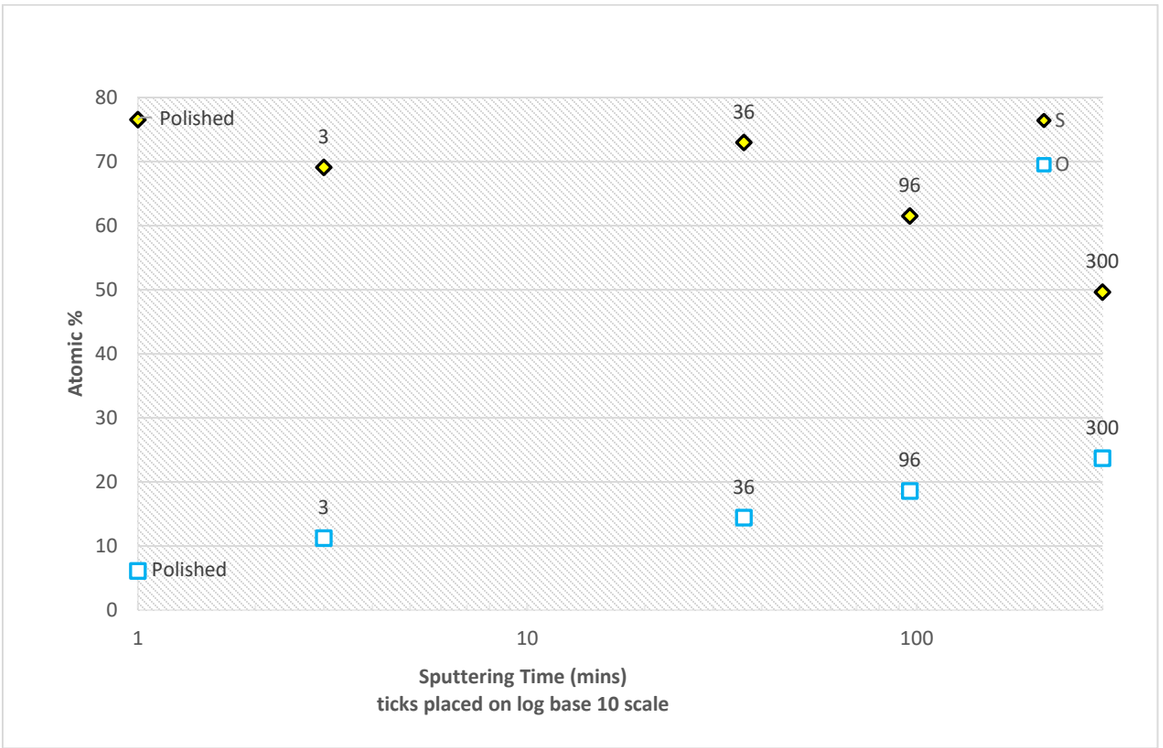

Figure 3.10: Logarithmic plot of sulfur and oxygen content from EDX spectra of the $WS_{2.7}$ target as a function of sputtering time.

Following sputtering use, rather than a circular region on the surface of the target being eroded as a result of the plasma, which was the case for stoichiometric target, the sulfur-rich target had an absence of such sputtering circular grove and exhibited a surface randomized selective sputtering of sulfur phase regions due to the high vapor pressure of unbonded sulfur. This resulted in random and non-uniform sized depressions appearing on the target surface, which also deepen over the sputtering time, as depicted in Figure 3.11. These regions become sulfur depleted as confirmed with EDX mapping in Figure 3.12.

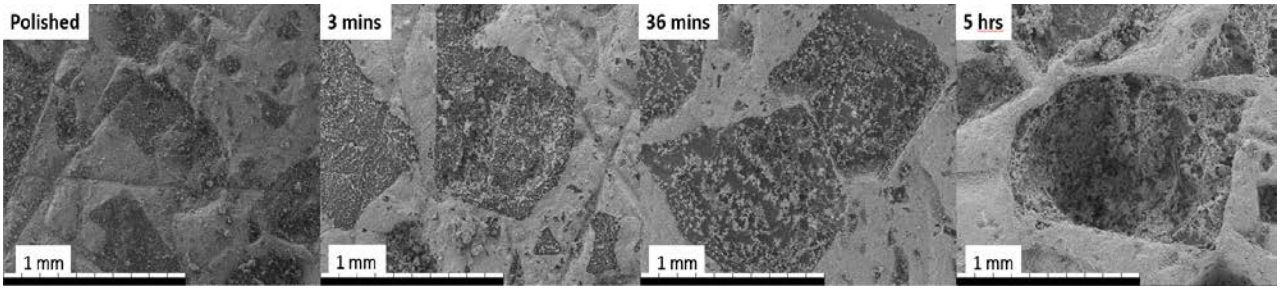

Figure 3.11: **SEM images of the $WS_{2.7}$ target after initial polishing, 3 minutes, 36 minutes, and 5 hours of sputtering use.**

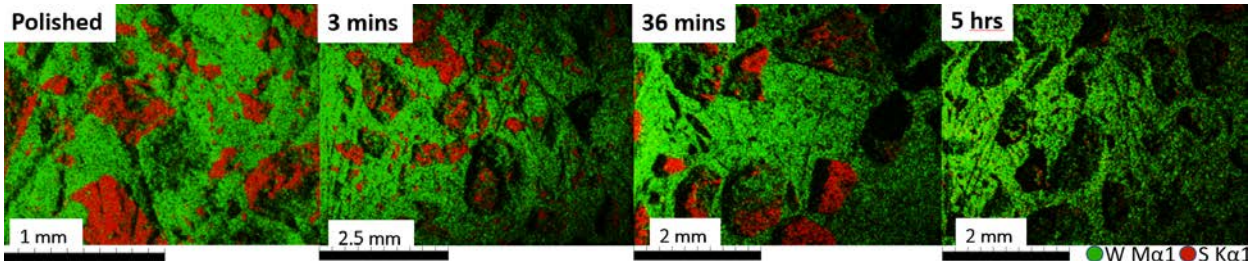

Figure 3.12: **EDX maps of $WS_{2.7}$ target sulfur-rich region's progression after sputtering use.**

The amount and density of the regions with sulfur phase selective sputtering and surface depressions was clearly detectable already after three minutes of sputtering. This could be caused from both biasing the target itself and the heat generated from the plasma at the targets surface which is much higher than the 75°C during sintering. It is then plausible that the lack of erosion groove on the $WS_{2.7}$ target surface can be explained by either the over-

stoichiometry itself or the high density of the sulfur phase segregates. Alternatively, the selective sputtering of the sulfur phase segregates could disrupt the typical for unbalanced magnetron ionization concertation caused by the high electron density following the circular magnetic field.[103] The sulfur high local pressure originating by randomized vaporization from the target surface segregated phases could randomize the gas ionization and lead to a more macroscopically uniform plasma distribution across the surface of the target. The localization of erosion at the sulfur-rich sites also led to forming metallic tungsten dendrites after first three minutes of sputtering, which have a higher electrical conductivity and hence the regions of electrical field concentrations from the imposed RF bias voltage, which do not follow the magnetic field pattern. A combination of these phenomena could be taking place and was suggested to explain the absence of the erosion groove on $WS_{2.7}$ target surface, as compared to stoichiometric target. We also note that a similar absence was noticed in our experiences with sulfur-rich $MoS_{3.6}$ targets.

As the sulfur phase is selectively sputtered, tungsten dendrites can also be seen at the base of the eroded depression regions. These dendrites grow larger as a function of the sputtering time, which can be seen in the nearly 10 um wide cluster formed after three minutes of sputtering in Figure 3.13.

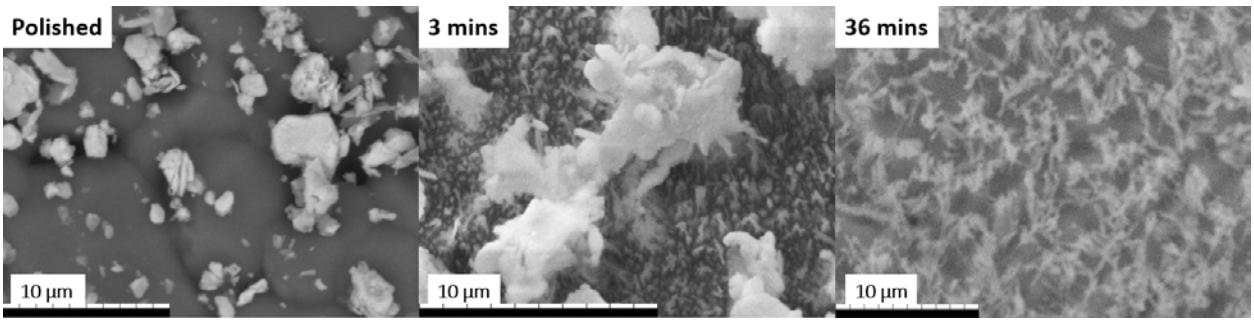

Figure 3.13: **SEM images of dendrite formation on $WS_{2.7}$ target.**

A chemical contrast within the sputtering depressions of the $WS_{2.7}$ target can be clearly identified in the EDX maps in Figure 3.14[1] with tungsten dendrites (Figure 3.14[2]) sitting above the base of the depression which is composed of 97% sulfur. The SEM image in Figure 3.14[3] depicts the morphology of the sulfur phase at the base of the depression after one hour and 36 minutes of sputtering time.

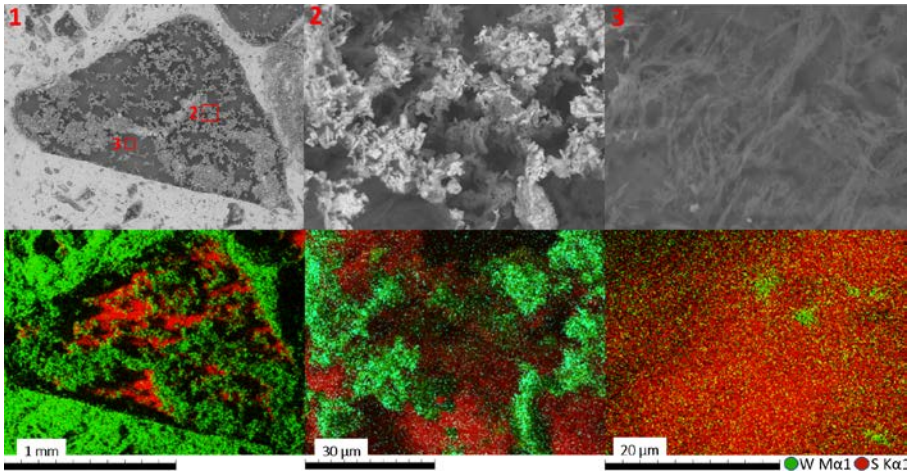

Figure 3.14: **SEM surface images and corresponding EDX maps obtained from the surface of $WS_{2.7}$ target sputtered 1 hour and 36 mins, illustrating large depressions (1) with tungsten dendrite growth (2) and sulfur-rich bottom (3), using different magnifications to locations indicated in SEM image a).**

To investigate if the observed phase segregation is limited to the surface only or also occur within the bulk of the target, additional studies were performed deeper into the target after five hours of sputtering time. First, the $WS_{2.7}$ target was removed from bonded copper backing plate and any remaining colloidal silver conductive paste was cleaned. The back face of the target was then investigated. Clear phase segregation was present, apparent from the EDX maps of Figure 3.15, but is much denser, smoother, and homogenous compared the unsputtered sulfur phases.

The $WS_{2.7}$ target was then fractured in half through its face in order to explore a cross-section of the sulfur phase depressions and tungsten dendrite evolutions shown in Figure 3.16.

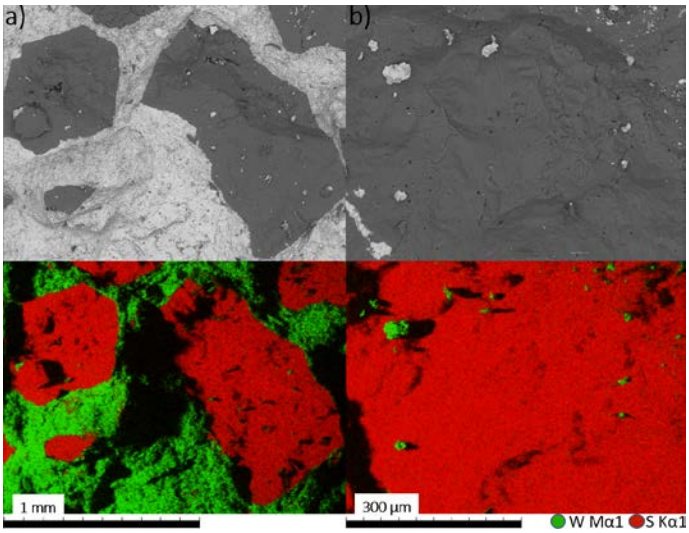

Figure 3.15: **EDX maps of sulfur segregates on back-side of $WS_{2.7}$ target after 5 hours sputtering.**

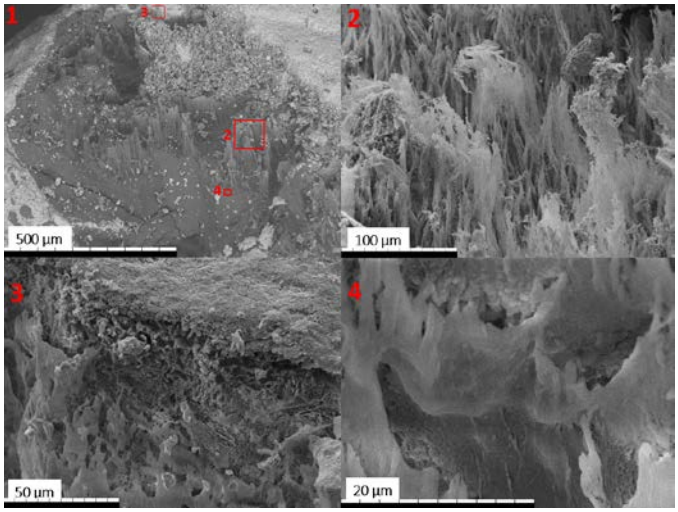

Figure 3.16: **Cross-fracture SEM image of depression in $WS_{2.7}$ target after 5 hours sputtering. BSE x120 of sulfur rich region with sites 1) SE x600 of dendrites, 2) SE x1200 of W grain boundary, 3) SE x5000 below dendrites.**

When the sulfur phase is selectively sputtered, the small percentage of tungsten present is left unsputtered, leaving behind porous dendrites and foams of tungsten that look similar to tungsten based nanoflakes prepared in Yuvasravan et al.[46] This small amount of tungsten present in the native sulfur is possibly interrelated to the formation of the elemental sulfur, where the oxidation of metals can catalyze the oxidation of elemental sulfur by oxygen.[104]

Further adding to this theory, the sulfur phase on the bottom of the $WS_{2.7}$ target has no tungsten in its matrix and has no discernable damage after five hours of sputtering. The sulfur phase grew in size and number of sites on the $WS_{2.7}$ target with increased sputtering use; progressing to the point where they are easily noticeable by eye and cause extensive damage across the whole surface of the target. This rapid increase in the elemental sulfur phase is likely caused by sulfur migration and oxidation of sulfur due to the biasing of the target and the energy added into the target over time through sputtering. The sulfur vacancies were filled by oxygen shown in Figure 3.10, which could have driven a runaway loop of oxygen catalyzing elemental sulfur which was then sputtered and replaced by more oxygen.

An analogous example to sulfur oxidation in the target over sputtering time is elemental sulfur growth reported for TMDs used in lithium-based batteries.[31], [46], [87-89], [104] The first recharge of a battery does not lead to complete polysulfide oxidation into elemental sulfur.[104] Instead, it takes an overcharge of the battery and several more charges of the sulfur electrode in order for high-order polysulfides to react, and several steps for the oxidation of the short chain polysulfides with the long chain polysulfides to form elemental sulfur.[104-105] The sulfur cathodes expand to a significant volume after charge cycling occurs, which also takes place in the $WS_{2.7}$ target from the considerable cavities left in the target that are visible in Figure 3.11 after five hours of sputtering.[31], [89] An explanation is required as to why the $WS_{2.7}$ target experiences this reaction while the commercial WS_2 target that similarly becomes sulfur-depleted shows no damage besides the typical erosion groove. The migration of the sulfur and formation of elemental sulfur in batteries is termed the “shuttle effect” of sulfur, and is dependent on both the total sulfur concentration (S_{total}) and the interaction between positively

charged sulfur vacancies (V_S) and negatively charged polysulfides.[31], [87-89], [104] These two factors could likewise explain why the stoichiometric WS_2 target suffers less damage, as it intrinsically has a lower sulfur concentration and would initially contain much more sulfur vacancies than its sulfur-rich counterpart. The sulfur vacancies act as traps for the polysulfides through adsorption while affecting their redox reactions by limiting active sites for polysulfide intermediates.[88] Other TMDs have been deemed more promising sulfur-rich hosts than WS_2, such as vanadium disulfide (VS_2) owing to high chemical adsorption of polysulfides, high polarity for catalytic sites, and conversion of the polysulfides.[31], 89]

3.2.2 Phase Analysis of the Target Surface

The phase analysis of the target surfaces was accomplished with Raman and XRD investigations, which were referenced to a stochiometric target surface for the phase evolutions. Characterizing the phase compositions of targets containing unbonded sulfur is challenging because of the several allotropes of sulfur crystals, the varying length of sulfur chains possible, and the wide array of different polysulfides that could be present.[104] As a background to our analysis of $WS_{2.7}$ target phases, elemental sulfur (denoted as either S_8 or S^0) can take the form orthorhombic native sulfur (α-sulphur) which is the most common form, a common monoclinic configuration (ß-sulfur, or an uncommon monoclinic form rosickyite (γ-sulfur).[107] To make matters more complex, the different polytypes of sulfur crystals can be unstable both chemically and structurally, and have been shown to form a mixture of a-, ß- and y-sulphur.[104], [107] This mixture of sulfur is also dynamic, as rosickyite is formed from molten sulfur that is slowly cooled, but rosickyite is meta-stable at room temperature and slowly reverts to native sulfur.[107] Sulfur also undergoes a cycle between elemental sulfur and

polysulfide chains/ions through sulfide oxidation, where the intermediate oxide species have many possible redox reactions.[104], [107] Proposed redox reactions describe the stepwise sulfur reduction of soluble polysulfide intermediates, which include unstable S^+ atoms at the end of polysulfide chains reacting with other polysulfide chains, while a split in the S-S chain would yield elemental sulfur.[108-109] Other proposed redox reactions involve negative polysulfide chains of increasing lengths combining and releasing electrons until elemental sulfur is generated.[87], [104], [106] Compounding the issues on a lack of consensus for the redox reactions themselves, the thermodynamic potential of forming any of the polysulfide intermediates is equal, meaning that any of the S_4^{2-}, S_4^-, and S_3^- are equally probable. Further, these reactions consume different sulfide species which can be in equilibrium with the polysulfide intermediates.[106-108]

In Raman spectroscopic analysis, crystalline sulfur's three allotropes share many vibrational features with few differences. Peaks at 153 cm^{-1}, 220 cm^{-1}, and 473 cm^{-1} are common between all the three allotropes, as well as a broad feature at ~440 cm^{-1} and a shoulder at ~467 cm^{-1}.[104] There are slight differences in the spectral features of the sulfur allotropes, such as a sharper peak at ~440 cm^{-1} for α-S8, broader peaks and a missing a peak at 248 cm^{-1} for ß-S8, γ-S8 displaying a shoulder at ~216 cm^{-1}, and inconsistent changes between intensity and FWHM for the ~150 cm^{-1} peak for all samples.[104] All samples displayed a more intense symmetric bending mode peak at ~220 cm^{-1} than the less intense asymmetric bending peak at ~150 cm^{-1}.[104] In general, the 100-800 cm^{-1} region of the spectra represents the asymmetric and symmetric S-S bending, as well as the S-S stretching vibrations for all three S8 allotropes.[104], [106] In order to find distinct vibrational differences in the spectra, analysis of low

frequency Stokes-shifts is required.[104] The Raman system used for this work has a low-frequency filter and as such this analysis could not be carried out. However, based on Table 3.9 which complied the Raman studies of the S8 allotropes in *Nims at al*.

Table 3.9: Raman peak assignment for sulfur from experimental data.

Peak Position (cm-1)	Assignment	Vibrational Mode	Reference
153	Elemental S	Asymmetric S-S bending	[77], [104], [107]
217-220	Elemental S (and S_8^{2-})	Bending mode of S8 ring	[77], [106-107]
234	S_4^{2-} (x=4~8)	Bending mode	[106]
~280	S_x^{2-} (x=4~8)	N/A	[107]
~320	S_x^{2-} (x=4~8)	N/A	[107]
~400	S_x^{2-} (x=4~8)	N/A	[107]
~440 (broad)	Elemental S	S-S stretching modes	[77], [104]
467 (shldr)	Elemental S (γ)	S-S bond stretching of the S8 ring	[104]
473	Elemental S (γ)	Symmetric S-S bending	[77], [104], [107]
518	S_4^-	N/A	[106]
534-535	S^{3-}	Symmetric stretching mode	[106-107]
766	S_x^{2-} (x=4~8)	N/A	[106-107]
1066	$S_2O_4^{2-}$	S-O stretching mode	[106]

The spectral features of the three S8 allotropes were tabulated from Nims et al.[104] and was recorded in Table 3.10. These features were required in order to differentiate the sulfur Raman results due to the shared peaks at ~150 cm^{-1} , 216 cm^{-1}, ~220 cm^{-1}, and ~440 cm^{-1}. Most differences in the sulfur spectra occur at sub 150 cm^{-1} Stokes shifts.

Figure 3.17 provides Raman spectroscopy comparison of the $WS_{2.7}$ target against the stoichiometric commercial WS_2 target before and after sputtering. Raman spectra of both W-S based targets were also recorded before and after polishing and at different features and phases within each target.

Table 3.10: Raman spectral features S8 allotropes.[104]

α-S8 peaks (cm-1)	ß-S8 peaks (cm-1)	γ -S8 peaks (cm-1)
N/A	N/A	15
N/A	N/A	22
28	N/A	N/A
N/A	33	33
44	42	41
51	N/A	N/A
63	60 (shldr)	68
82	82	83
88	N/A	85
~150	~150	~150
216	216	216 (shldr)
~220	~220	~220
248	N/A	248
~440	~440	~440
N/A	N/A	468 (shldr)
N/A	N/A	473 (broad)

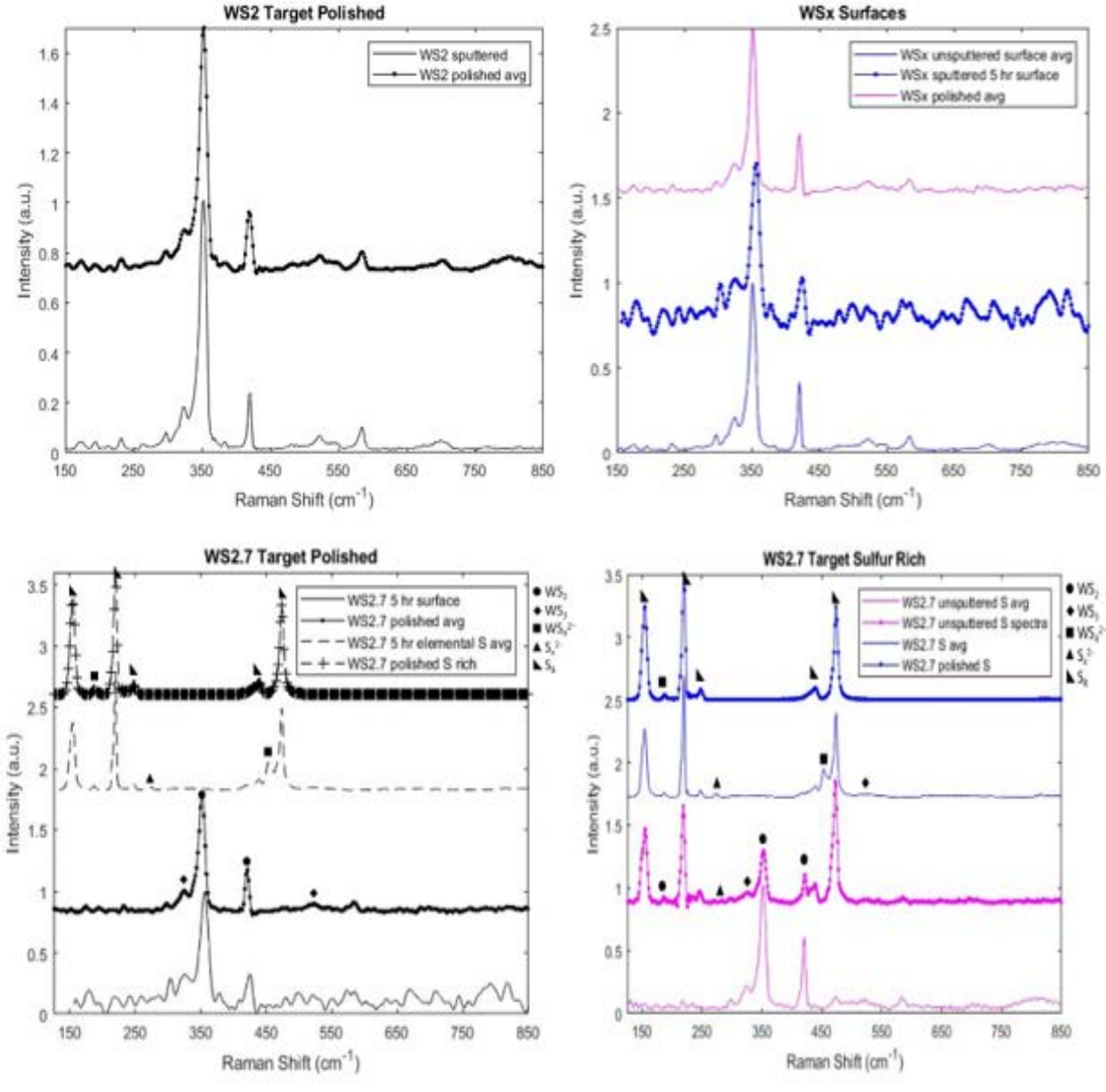

Figure 3.17: **Raman vibrational modes of the W-S based targets.**

Based on Table 3.10 which complied the Raman studies of the S8 allotropes in *Nims at al*, [104] the crystalline sulfur present in the $WS_{2.7}$ target can be assumed to be γ-S8 due to symmetric S-S bending at 473 cm^{-1} and the shoulder at 467 cm^{-1}. No ß-S8 was detected due to peaks present at 248 cm^{-1}. Additional evidence of γ-S8 are the pale needles at the bottom of the sulfur-phase depression in Figure 3.14[3] which likely forms after sputtering one hour and 36 mins due to the high temperatures the sulfur at the target surface experiences from ion-bombardment that is then slowly vacuum cooled. The crystalline sulfur containing a mixture of α- and γ-S8 cannot be ruled out since the features specific to α-S8 are almost indiscernible from γ-S8 besides the γ-S8 specific peaks. Moreover, it is known that the γ-S8 will eventually transition to α-S8 at room temperature. A mixture being present can be seen optically by the different oxidation states of the elemental sulfur in Figure 3.18 and looks markedly similar to the sulfur cathode with various polysulfides present in Jin-Tak Yeon et al.[107]

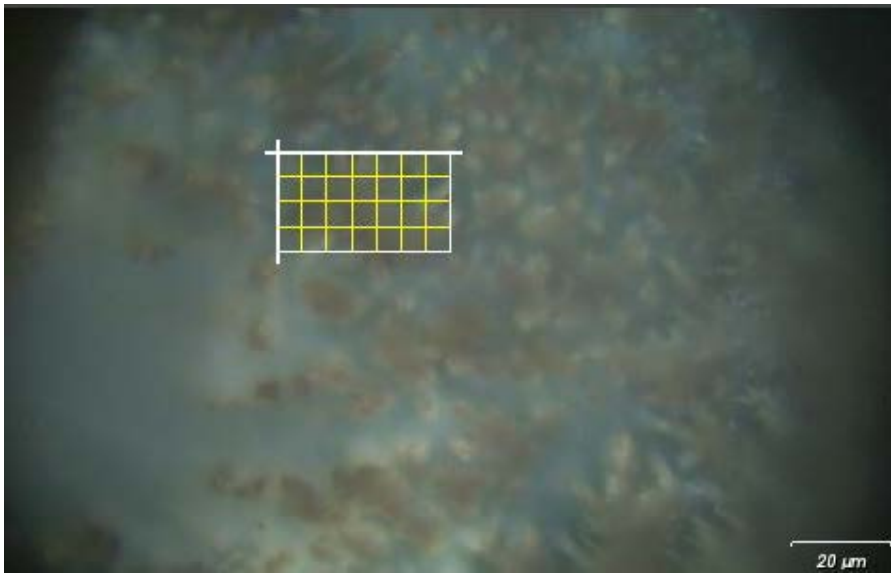

Figure 3.18: Optical image of native sulfur phase of the $WS_{2.7}$ target.

In our Raman analysis, the W-S based targets all displayed WS_2 first-order, second-order, and a combination of vibrations throughout sputtering and polishing at 176 cm^{-1} for of

LA(M), at 190 cm^{-1}, at 213 cm^{-1}, at 230 cm^{-1} for A_{1g}(M)-LA(M), at 264 cm^{-1} for 2LA(M)-$3E^2_{2g}$(M), at 297 cm^{-1} for 2LA(M)-$2E^2_{2g}$(M), a shoulder at 312 cm^{-1}, at 324 cm^{-1}, at 350-351 cm^{-1} for 2LA(M), at 355 cm^{-1} for E^1_{2g}(Γ), at 420 cm^{-1} for A_{1g}(Γ), at 523 cm^{-1}, at 582 cm^{-1} for A_{1g}(M)+LA(M), and at 704 cm^{-1} for 4LA(M) Many of these combinational vibrational modes were surprising as they are reported for 2D WS_2 samples at resonance.[38], [100] For example, the vibrational mode experimentally recorded at 324 cm^{-1} is not near any other phonon mode and has been assigned to the E˝ vibrational process in literature and is often reported as resonant excitation for TMDs but is sometimes undetectable due to the orientation of detectors.[100] Further, the features at 582 cm^{-1} and 704 cm^{-1} combined processes A_{1g}(M)+LA(M) and 4LA(M) which are observed in the scattering spectrum for monolayer WS_2.[100]

The unsputtered $WS_{2.7}$ target showed the only sign of surface oxide formation with WO_3 broad peaks at ~700 cm^{-1} and ~800 cm^{-1} but this was due to the target sitting in storage for some time and the oxide was removed after a three minute pre-sputter.[101] No other vibrational modes or species were detected for the WS_2 target after sputtering or polishing. Raman acquisitions of the sulfur-phase in the unsputtered $WS_{2.7}$ target show two intermediate sulfur-rich species; one within a WS_2 matrix, and one within an α-S8 matrix. The sulfur-rich WS_2 intermediate species has a peak at 234 cm^{-1} for S_4^{2-} polysulfide and all the resonant WS_2 vibrations besides LAM at 176 cm^{-1}, 213 cm^{-1}, A_{1g}(M)-LA(M) at 230 cm^{-1}, and 4LA(M) at 704 cm^{-1}.[77] The α-S8 intermediate species has the three elemental sulfur S-S bending and stretching vibrational modes, and does not yet show the γ-S8 vibrational modes. The α-S8 intermediate species also has all the resonant WS_2 vibrational modes besides LAM at 176 cm^{-1}, 190 cm^{-1}, 213 cm^{-1}, A_{1g}(M)-LA(M) at 230 cm^{-1}; while also having a WS_3 peak at 460 cm^{-1}, a WS_4^{2-} peak at 182

cm^{-1}, a $WO_2S_2^{2-}$ peak at 432 cm^{-1}, and polysulfide peaks at 234 cm^{-1} for S_4^{2-} and at ~280 cm^{-1} for S_x^{2-} (x=4~8).[77] After sputtering and polishing the $WS_{2.7}$ target shows no major spectral differences besides the elemental sulfur-phase. After five hours of sputtering, the elemental sulfur phase in the $WS_{2.7}$ target is now comprised of a mixture of α-S8 and γ-S8 with new shoulders at 216 cm^{-1} and 467 cm^{-1} for S-S bond stretching of the γ-S8 ring. The phase still contains polysulfides as well as a new WS_4^{2-} peak at 455 cm^{-1} and two new WS_3 vibrational modes at 330 cm^{-1} and 530 cm^{-1}.[77] During the sulfurization of WO_3/Al_2O_3 in Payen at al, WS_3 is also formed as an intermediate with an oxysulphide species during the oxidation of sulfur.[77] The oxidation of the sulfur was proposed to change in the intermediates from WS_2 → WS_3 → oxysulphide → oxide.[77] After polishing, some of the elemental sulfur phase in the $WS_{2.7}$ target still contains γ-S8 based on the shoulder at 467 cm^{-1} remaining. No more WS_3 peaks remain, and the only WS_2 vibrational mode is at 190 cm^{-1}. Some of the sulfur-phases contained a S_4^{2-} bending mode at 234 cm^{-1}, and others had WS_3O^{2-} vibrational modes at 182 cm^{-1} and 878 cm^{-1}.[77]

The A_{1g}(Γ) peak location, E′ line location, peak ratios, and distance from one another are commonly correlated to film thickness.[24], [37-38], [54] These factors were determined for the WS_2 and $WS_{2.7}$ Raman spectra in order to validate their effectiveness. It has been reported that the E^1_{2g}(Γ) phonon mode redshifts and the A_{1g}(Γ) mode blueshifts for an increasing number of layers, and the distance between these peaks can also identify the number of layers.[37] However, these factors gave conflicting values of thickness for the bulk sputtering targets. The A_{1g}(Γ) peak locations for the commercial WS_2 target varied from 419-421 cm^{-1} after sputtering and polishing. The A_{1g}(Γ) peak locations for $WS_{2.7}$ also varied from 419-422 cm^{-1} for unsputtered,

sputtered, and polished spectra. Based on literature, an $A_{1g}(\Gamma)$ peak position of 419 cm^{-1} is reported as three-layers, 420 cm^{-1} is bulk, while 421 cm^{-1} is "multi-layered" and 422 cm^{-1} is not reported.[24], [37-38] The broad E′ line position was recorded by its highest relative intensity across multiple spectral acquisitions and maps, and the E′ line position for the commercial WS_2 target was roughly 353 cm^{-1} before and after polishing which does not have a reported correlated thickness in literature. The E′ line position for the unsputtered $WS_{2.7}$ target was at 350-351 cm^{-1} which fluctuates from monolayer, two-layer, and bulk.[38] After the $WS_{2.7}$ target was sputtered for five hours the E′ line position was at 355-356 cm^{-1} and after polishing the E′ line position was at 351-352 cm^{-1}, which again is reported as monolayer, two-layer, and bulk.[38] The E line position at 353 cm^{-1} for the WS_2 target before and after polishing was assigned the $E^1_{2g}(\Gamma)$ mode. The unsputtered $WS_{2.7}$ target's E′ line position was the 2LA(M) mode at 350-351 cm^{-1}, but after sputtering it shifted to the $E^1_{2g}(\Gamma)$ mode at 355-356 cm^{-1}, and again after polishing it transitions back to 2LA(M) at 351-352 cm^{-1}. The $WS_{2.7}$ target had a 2LA(M) to $A_{1g}(\Gamma)$ distance of 69 cm^{-1} before sputtering, an $E^1_{2g}(\Gamma)$ to $A_{1g}(\Gamma)$ distance of 69-70 cm^{-1} after sputtering for five hours, and a 2LA(M) to $A_{1g}(\Gamma)$ distance of 70 cm^{-1} after polishing; which are all reported as bulk.[37-38] The $E^1_{2g}(\Gamma)$ to $A_{1g}(\Gamma)$ distance for the commercial WS_2 target was 68 cm^{-1} after sputtering which is reported as three-layers, and after polishing was 66 cm^{-1} which is reported as monolayer.[37-38] The 4 cm^{-1} difference between the recorded peak distances for the WS_2 and $WS_{2.7}$ targets is comparable to the roughly 4-5 cm^{-1} distance between the 2LA(M) and $E^1_{2g}(\Gamma)$ peaks. This confirms the $E^1_{2g}(\Gamma)$ mode does in fact dominate the E' line overlap for the WS_2 target, and that the 2LA(M) mode dominates the E' line overlap for the $WS_{2.7}$ target. The E'

line:A_{1g}(Γ) peak intensity ratio was calculated for the WS_2 and $WS_{2.7}$ targets to distinguish if this factor would accurately determine thickness. All peak intensity ratios in this work use a ratio of the highest E′ line intensity to the A_{1g}(Γ) peak intensity. Therefore, the 2LA(M) mode is assigned to the highest intensity of the E′ line between 351-353 cm^{-1}, and the E^1_{2g}(Γ) mode is assigned for intensities of the E′ line between 355-356 cm^{-1}. Peak ratios of the targets vary widely from 2:1 which is monolayer, 1:1 which is two-layers, 4.48:1 which is significantly higher than monolayer, and even some non-integer layers of WS_2. Not a single scan on the W-S based targets produced a peak ratio agreeing with bulk.[38]

The factors calculated from the Raman spectra did not accurately predict the thickness of the W-S based targets. A_{1g}(Γ) peak location as an indicator of film thickness is far too narrow, with a slight shift in between scans on the same sample being the difference between monolayer and bulk. Using the E′ line location, peak ratios, or E′ line to A_{1g}(Γ) peak distance for thickness are predicated upon deconvoluting or assigning vibrational modes between the E^1_{2g}(Γ) and 2LA(M) overlap in the E′ line, which sabotages the whole process. None of these factors were consistent in determining the number of layers, nor did their results agree with each other. Ultimately these factors require precise Raman spectra due to their very fine line separating the number of layers, and any slight shift in value from any other material property or sample parameters would lead to inaccurate results such as the disagreement with the bulk W-S based samples.

The E′ line and A_{1g}(Γ) peak intensities and the E′ line:A_{1g}(Γ) peak intensity ratio have been correlated to the level of crystallinity and lattice defects within a crystalline sample.[24], [37-38], [54]

Tan et al. correlates a $WS_{2.64}$ hybrid sample of and the ratio of its peaks to oxygen defects which were seen in SEM images and were confirmed by XPS.[45] A similar approach but for sulfur defects was attempted after visibly seeing damage to the sulfur phase in SEM images and EDX scans and later confirming sulfur content with XPS. The sulfur content was found to increase as the E' line:A_{1g}(Γ) peak intensity ratio decreased, which was accurate in comparing i) the W-S based targets against each other, ii) the same target at different positions (such as at sulfur-rich positions with known S:W ratios), and iii) for the same target after sputtering and after polishing. The WS_2 commercial target had an E^1_{2g}(Γ) to A_{1g}(Γ) intensity ratio of 4.42 after sputtering and 3.82 after polishing, which agrees with the S:W ratio of 1.3 after sputtering and 1.7 after polishing. The unsputtered $WS_{2.7}$ target has a 2LA(M) to A_{1g}(Γ) intensity ratio of 2.42 and sulfur-rich phases with ratios of 1.72-1.76, which is again in agreement with the trend. After sputtering the intensity ratio increases to 3.07, and the sulfur-rich phase spectra shows the first instance where the A_{1g}(Γ) peak is more intense than the E' line with a ratio of 0.78, which is presumably caused by the further oxidation of the sulfur as a result of sputtering. After polishing, the $WS_{2.7}$ target nearly returns to a ratio of 2.42, with a 2LA(M) to A_{1g}(Γ) intensity ratio of 2.66; which is also in agreement with near-full restoration of the sputtering target after polishing.

It is not known exactly which sulfur defect most effects the peak intensity ratios, but it is likely sulfur interstitials or the shorter S_x^{2-} polysulfides. These sulfur species also likely induced the double resonance of the 2LA(M) vibrational mode, and why the stoichiometric WS_2 target is more intense in the E^1_{2g}(Γ) vibrational mode. The only chemical species that would likewise

explain the transition in intensity from 2LA(M) to $E^1_{2g}(\Gamma)$ after sputtering and reverting back to 2LA(M) after polishing is S_4^{2-}, based on its vibrational bending mode at 234 cm^{-1}. S_4^{2-} is present in the sulfur-rich phase of the unsputtered $WS_{2.7}$ target and after polishing, but is not detected after the sample is sputtered for five hours.

As for the general resonance that occurred, Berkdemir et al. report their 2D samples only reached resonance near the 512 nm laser that was used. A 532 nm laser was used for this work, which has also been used to generate resonance, but these targets are at least 1 cm thick.[37-38] The entire profile of the Raman spectra depends on the phonon excitation energy, where conditions for double resonance of a second-order phonon process highly depend on the optical excitation energy equaling a band transition.[38], [100] Therefore, starting with a very fine polycrystalline target with many different orientations available and averaging spectra from a large map scan using a 532 nm laser at its lowest power setting, could generate the exciton-phonon interaction to achieve detectable resonance. Ultimately, resonant conditions are material dependent and are not common across TMDs, and may vary from sample to sample.[100] Further study is required and is outside the scope of this work.

Figure 3.19 presents results of XRD analysis for the investigations of phases of the $WS_{2.7}$ target and their comparisons against the stoichiometric commercial WS_2 target before and after sputtering. The crystal structure of both W-S based targets was recorded before and after polishing, and at different features and phases within each target.

From the measured interplanar (002) spacing from the corresponding diffraction peak at 2Θ=14.2 degrees, the peak FWHM and crystallite size were calculated using the Scherrer formula which are presented in Table 3.11.

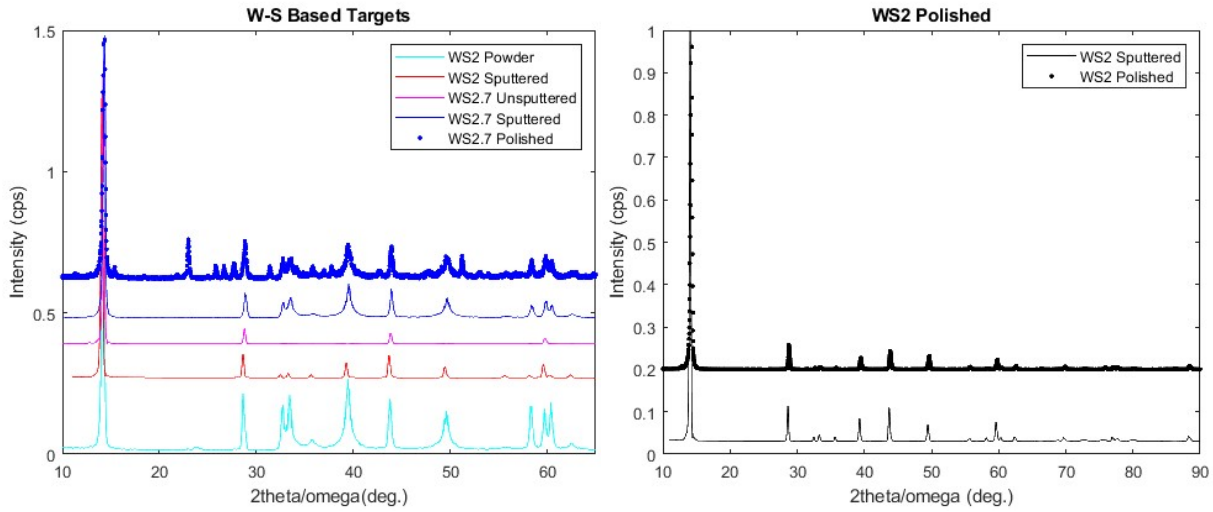

Figure 3.19: **Diffraction patterns from coupled 2theta/omega XRD scans of sputtering targets.**

Table 3.11: W-S Target XRD interplanar spacing, peak FWHM, and crystallite size which was calculated with the Scherrer equation.

Sample Status	(002) D Spacing [A]	FWHM	Crystallite Size [nm]
WS_2 sputtered	6.2852	0.236	46
WS_2 polished after sputtering	6.2233	0.278	37
$WS_{2.7}$ unsputtered	6.2229	0.215	51
$WS_{2.7}$ sputtered five hours	6.1963	0.29	38
$WS_{2.7}$ polished after sputtering	6.1889	0.292	35

In the XRD analysis, the W-S based targets all displayed a dominant (002) hkl peak of hexagonal WS_2 phase, and shared all bulk poly-crystalline diffraction peaks with the original WS_2 powder and other XRD patterns from literature.[39], [44] Both the $WS_{2.7}$ and WS_2 targets had no distinguishable change in the WS_2 diffractions after sputtering or after polishing and no tungsten oxide diffraction peaks were observed in the XRD spectra.[39], [43] The interatomic spacing of the $WS_{2.7}$ and WS_2 commercial targets are comparable before and after polishing, and both show a decrease in strain after polishing. The targets' crystallinity was also virtually the same.

The XRD analysis of the targets only displayed sulfur diffraction peaks in the $WS_{2.7}$ target and none of these were present in the control WS_2 target. The sulfur crystal structure diffraction peaks were most easily observable between 20-30˚ in Figure 3.19 (left). These features were very minor for the unsputtered $WS_{2.7}$ target, then become almost entirely diminished after five hours of sputtering. However after polishing, the sulfur peaks reach the highest relative intensity. The sulfur phase XRD peak intensification after experiencing both sputtering and polishing demonstrates the growth and oxidation of the crystalline sulfur as a direct result of sputtering. The sulfur phase in the $WS_{2.7}$ target exhibits the same peaks as the original sulfur powder (except the relative intensities and their relationship to each other are much different). The sulfur seems to exhibit diffractions consistent with orthorhombic sulfur, and rosickyite diffraction peaks are not detected which may be due to the high absorption of X-rays by the crystal.[110]

3.2.3 Chemical Bonding of W and S in Sulfur Rich Targets

The W-S based target's bonding environment and chemical composition were confirmed through XPS. Figure 3.20 presents high resolution XPS original and deconvoluted peak fitted spectra of both W 4f and S 2p orbitals from the WS_2 target after five hours of sputtering and then again after polishing. The C 1s peak was used as a reference. Table 3.12 presents the results of an elemental percentages of W, S, and O from in the WS_2 target after five hours of sputtering and then again after polishing, obtained from XPS survey spectra analysis.

Table 3.12: **XPS derived elemental percentage composition of WS_2 target.**

Target Status	W (4f)	S (2p)	O (1s)	S:W
Sputtered 10+ hrs	19.2%	25.2%	55.6%	1.3
Polished	28.8%	51.6%	19.6%	1.8

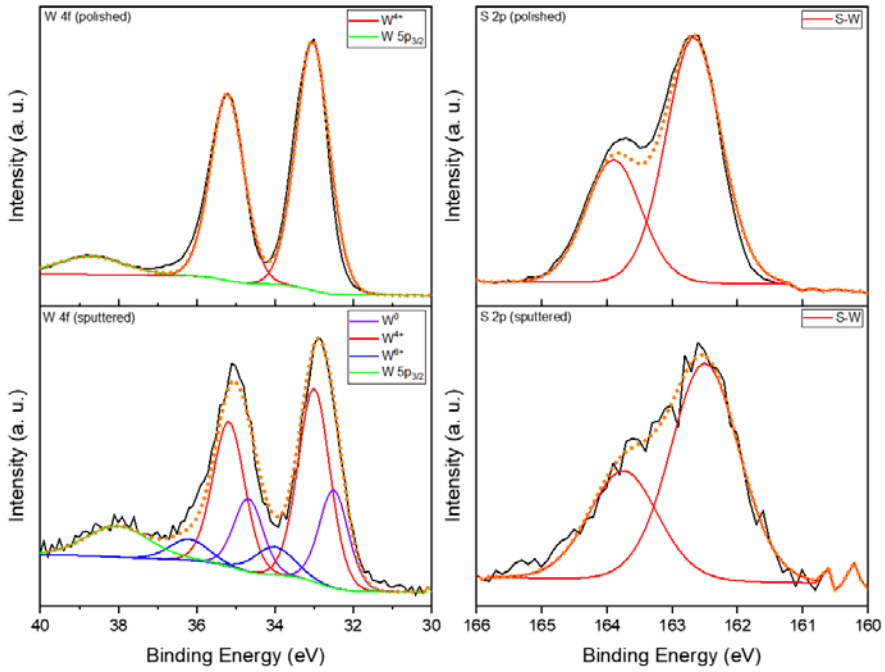

Figure 3.20: XPS spectra in W 4 f and S 2 p spectral regions with deconvolution of WS_2 commercial target after sputtered over 10 hours, and polished WS2 target respectively.

XPS analysis revealed that after extensive sputtering the WS_2 target has several oxidation states of tungsten, featuring a doublet due to metallic tungsten, another doublet for W^{4+} that reflects stoichiometric WS_2 bonding, and higher binding peaks of W^{6+} that are indicative of a WO_3 oxide on the sulfur-depleted surface. The presence of metallic tungsten after extensive sputtering use gives credence to the theory of the tungsten acting as a catalyst for sulfur oxidation. During the sputtering, the TMD target will be sub-stoichiometric after 1-2 seconds of a plasma being introduce due to depletion of the chalcogen atoms, but the metal surface should then be exposed to more impinging argon atoms and thus the metal atoms will resultingly increase their yield to equal that of the chalcogen atoms; causing a steady-state of target stoichiometry over time to be reached.[49] Instead, equilibrium was not reached and metallic tungsten remains, possibly as sulfur oxidation by-products which led to more sulfur being sputtered than the tungsten. After polishing the WS_2 target, the W^0 and W^{6+} oxidation

states disappear from the spectrum, indicating that the metal-rich surface and oxides were mechanically removed. The sulfur S^{2-} oxidation state remains relatively unchanged for the S 2p orbital besides a more resolved spectra after polishing. The S:W ratio is almost fully restored for the commercial WS_2 target; from 1.3:1 to 1.8:1. The commercial WS_2 target does not return back to its fully stoichiometric 2:1 S:W ratio, which could be due to sulfur leaching throughout the whole target, but it is more likely that the target was not fully polished through the sulfur-depleted region.

High resolution XPS spectra of the deconvoluted W 4f and S 2p orbitals from the $WS_{2.7}$ target after five hours of sputtering and then again after polishing are depicted in Figure 3.21. Elemental survey percentages of W, S, and O from the $WS_{2.7}$ target were obtained after five hours of sputtering and then again after polishing obtained from XPS survey spectra analysis can be found in Table 3.13.

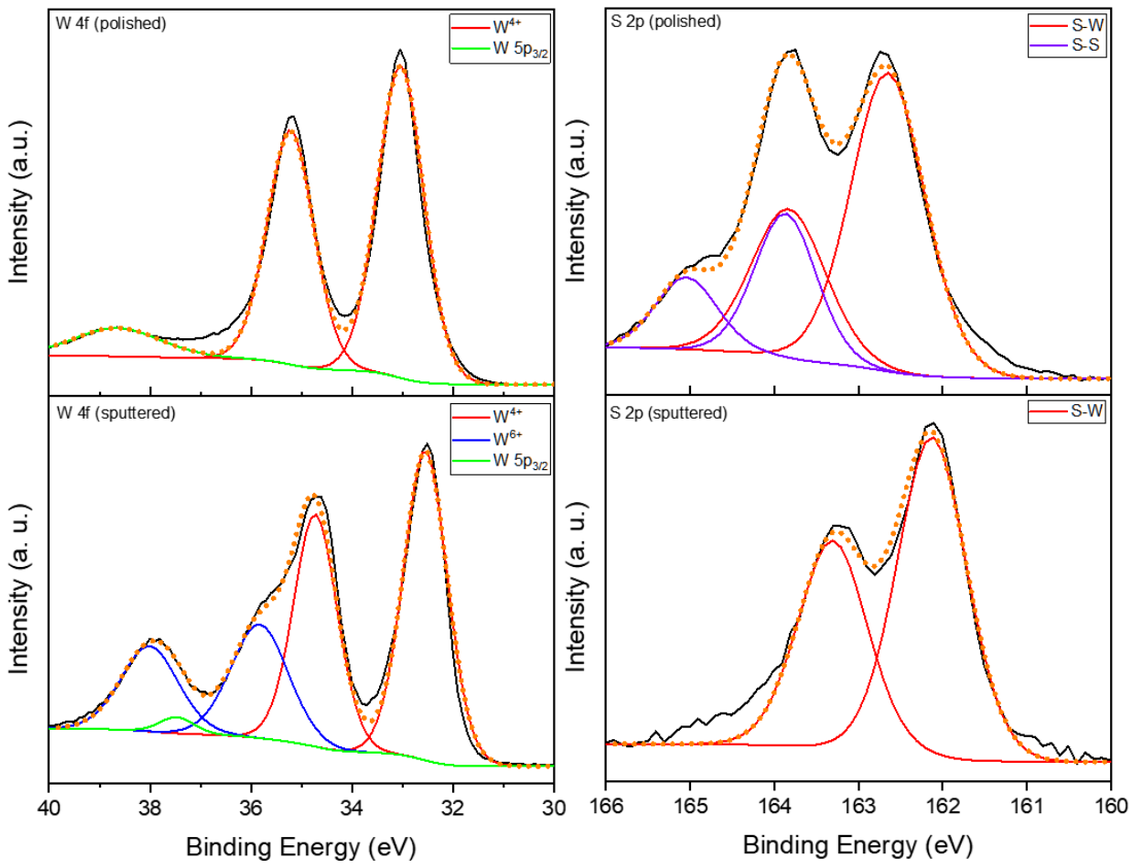

Figure 3.21: **XPS spectra in W 4 f and S 2 p spectral regions with deconvolution of $WS_{2.7}$ target after sputtered 5 hours, and polished $WS_{2.7}$ target respectively.**

Table 3.13: **XPS derived elemental percentage composition of $WS_{2.7}$ target.**

Target Status	W (4f)	S (2p)	O (1s)	S:W
Sputtered 5 hrs	18.4%	24.8%	56.8%	1.4
Polished	25.6%	68.3%	6.1%	2.7

After five hours of sputtering $WS_{2.7}$ target exhibits two oxidation states of tungsten, with the doublet for W^{4+} distinctive of WS_2, and the higher binding energies of W^{6+} which could again signify WO_3 or could corroborate the Raman results of the existence of WS_3 that was also found in the target five hours after sputtering. The S 2p orbital of the $WS_{2.7}$ target after five hours of sputtering only shows the S^{2-} oxidation state, similar to the WS_2 target, but polishing exposes a S-S bond. This result further substantiates the Raman results of a S_4^{2-} species being present before sputtering, being absent after five hours of sputtering, and replenished after polishing. The sulfur-rich $WS_{2.7}$ target undergoes a complete restoration of S:W ratio, from 1.4:1 after five hours of sputtering back to its original 2.7:1 after polishing. XPS analysis confirmed the EDX results of a near 1:1 replacement of sulfur with oxygen in both targets. Upon polishing both targets the thick oxide layers were removed, revealing the untarnished sulfur layers below.

3.3 Laser Annealing of Sulfur-Rich Precursors

3.3.1 Chemical Composition of Amorphous Films

The film's bonding environment and chemical composition were confirmed through XPS. For the deconvolution of the XPS peaks, multiple oxidation states of molybdenum and sulfur were considered with positions of Mo 3d and S 2p duplets summarized in Table 3.14 and compared to the positions of these oxidation state peaks as reported in L. Benoist et al.[64]

Table 3.15 likewise references the binding energies of oxidation states of sulfur in its S 2 p orbital with the chemical compounds the oxidation states are found in.[64] Figure 3.22 presents high resolution XPS original and deconvoluted peak fitted spectra of both Mo 3 d and S 2p orbitals from the amorphous films before laser annealing.

Table 3.14: Binding energies of Mo 3d orbitals from XPS data of MoS_x films.[64]

Compound	Species	Mo $3d_{5/2}$	Mo $3d_{3/2}$
MoS_2	Mo^{4+}	229.5 – 229.6	232.6 – 232.8
MoO_2	Mo^{4+}	229.6	232.6
MoS_3	Mo^{5+}	229.3 – 230.8	232.6 – 234.1
MoO_3	Mo^{6+}	232.6 – 232.7	235.8 – 235.9

Table 3.15: Binding energies of S 2p orbitals from XPS data of MoS_x films.[64]

Compound	Species	Mo $3d_{5/2}$	Mo $3d_{3/2}$
MoS_2	S-Mo	162.4 – 162.5	163.6 – 163.8
MoS_3	$(S_2)^{2-}$	162.2 – 163.4	164.6 – 164.7
MoS_3	S^{2-}	161.7 – 161.8	162.9 – 163.0

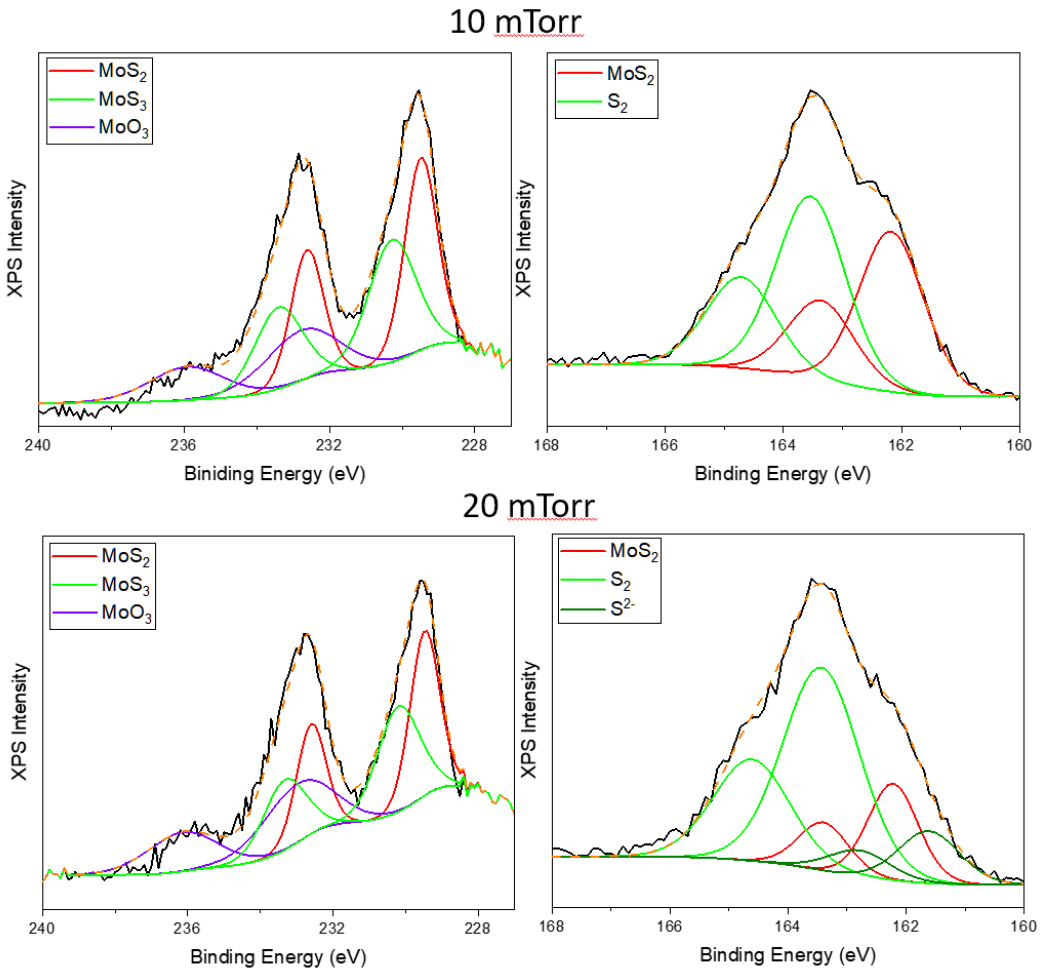

Figure 3.22: **XPS spectra in Mo 3 d and S 2 p spectral regions with deconvolution of MoS_x amorphous films sputtered on ITO-coated glass at working pressures of 10 mTorr and 20 mTorr, respectively.**

The molybdenum atoms in the MoS_3 compound have a Mo^{5+} oxidation state due to the bonding proposed by $Mo^{5+}[(S_2)^{2-}]_{1/2}(S^{2-})_2$ (s) from Benoist et al. and Liang et al.[64], [70] From this deconvolution, the fraction of MoS_3 present in the overall MoS_x film was calculated by the ratio of the Mo^{5+} to the S^{2-} and $(S_2)^2$ oxidation states in Table 3.16. The results of an elemental percentage survey scan present the composition of the MoS_x films in Table 3.17.

Table 3.16: XPS derived compound percentage MoS_x films sputtered on ITO-coated glass at working pressures of 10 and 20 mTorr.

Compound	10 mTorr	20 mTorr
MoS_2	39.7%	35.9%
MoS_3	36.8%	33.5%
MoO_3	23.5%	30.6%

Table 3.17: XPS derived elemental percentage composition of MoS_{2+} films sputtered ITO-coated glass at working pressures of 10 and 20 mTorr.

Element	10 mTorr	20 mTorr
Mo	16.67%	13.55%
S	39.82%	33.60%
O	43.51%	52.86%
S:Mo	2.39	2.49

The MoS_x films sputtered from the $MoS_{3.6}$ target were confirmed to be sulfur-rich by XPS elemental scans in Table 3.17 where the S:Mo ratios were 2.39:1 and 2.49:1 for the growth at 10 and 20 mTorr working pressure, respectively. The increase in S:Mo ratio between 10 and 20 mTorr was expected as increasing working pressure tends to increase TMD film's transition metal to chalcogen ratio.[49] The relatively high amount of oxygen that was also present for both working pressures originates from both the incorporation of residual water pressure in the sputtering chamber during film growth and from surface absorbents accumulated during film exposure to laboratory air before XPS analysis.

3.3.2 Laser Annealing of Amorphous MoSx Films and Raman Analysis

The substrates selected for the precursor film growth had the most profound effect on the film crystallization in the laser annealing processing step. Therefore, the laser annealing results presented below are organized by the used substrate. The crystallization was assessed through Raman spectroscopic analysis of the characteristic E^1_{2g} and A_{1g} 2H-MoS_2 peaks.

3.3.3 Annealing of MoS_x Films on ITO-Coated Glass Substrates

The MoS_x films deposited at working pressures of 10 and 20 mTorr onto ITO-coated glass were the first samples laser annealed in this work in order to determine if the chemical compositions of the films determined by XPS had an effect on laser induced phase transformations. The amorphous precursors were annealed at 100 mJ for one, five, and ten pulses. All films prepared at the 10 mTorr working pressure remained amorphous for all number of pulses. The 20 mTorr samples annealed at 100 mJ for ten pulses were crystallized to 2H-MS_2 as evidenced by the characteristic duplet of E12g and A1g peaks in Figure 3.23.

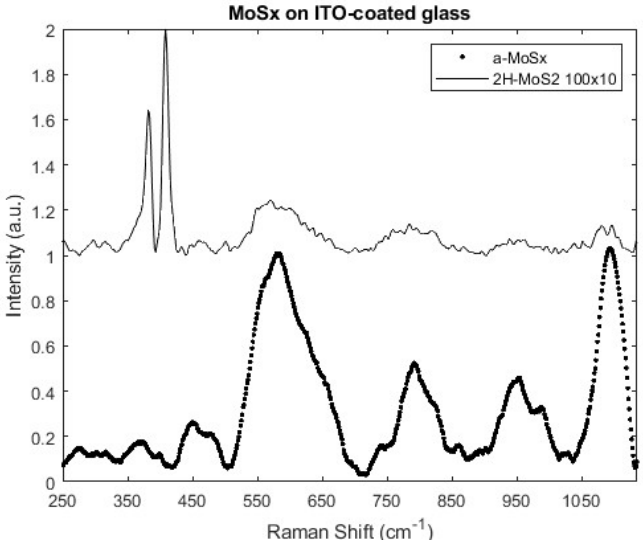

Figure 3.23: **Raman spectra of vibrational modes of MoS_x sample films on ITO-coated glass after being laser annealed at 100 mJ for ten pulses. The spectrum from the amorphous precursor film is included for a reference.**

The crystallinity of the films was correlated by the positions of the E^1_{2g} and A_{1g} peak positions as was done successfully for MoS_3 by C.H. Chang et al. where they determined the peak locations for x-MoS_2 (where x denotes a very crystalline film) and the peak locations of px-MoS_2 (where px denotes a poorly crystalline film).[75] The 2H-MoS_2 on ITO had a high degree of crystallinity as shown in Table 3.18.

Table 3.18: **Raman shifts of MoS_x films on ITO-coated glass substrates after laser annealing.**

Raman Modes	100x10	x-MoS_2	px-MoS_2
E12g	382	386	380
A1g	408	408	405.5

Despite the higher percentage of MoS_2 and MoS_3, and a lower proportion of MoO_3, the 10 mTorr samples retained the amorphous character of the films. Thus, all films thereafter were deposited using the 20 mTorr working pressure conditions.

3.3.4 Annealing of BON Encapsulated MoS_x Films on ITO-Coated Glass Substrates

The MoS_x films were encapsulated with BON, where BON serves several functions:

- Preventing MoS_x film from being physically damaged from scratching
- Preventing MoS_x from oxidation and water absorption in exposure to humid air
- Protecting MoS_x film during laser annealing from film ablation/delamination, oxidation, and sulfur-depletion by evaporation

The encapsulated films were annealed at 100, 200, 300, 400, and 450 mJ for one pulse each. At 100 mJ after one pulse, the films had equal regions of oxides MoO_2 and MoO_3 and elemental sulfur phase as shown in Figure 3.24. At 200 mJ, the samples contained the same amount of elemental sulfur and, in addition, a 2H-MoS_2 of crystallinity was detected from the E^1_{2g} and A_{1g} duplet. The amorphous BON also unexpectedly transitioned to h-BN at 100 and 200 mJ based

on its peak at 1350 cm^{-1}.

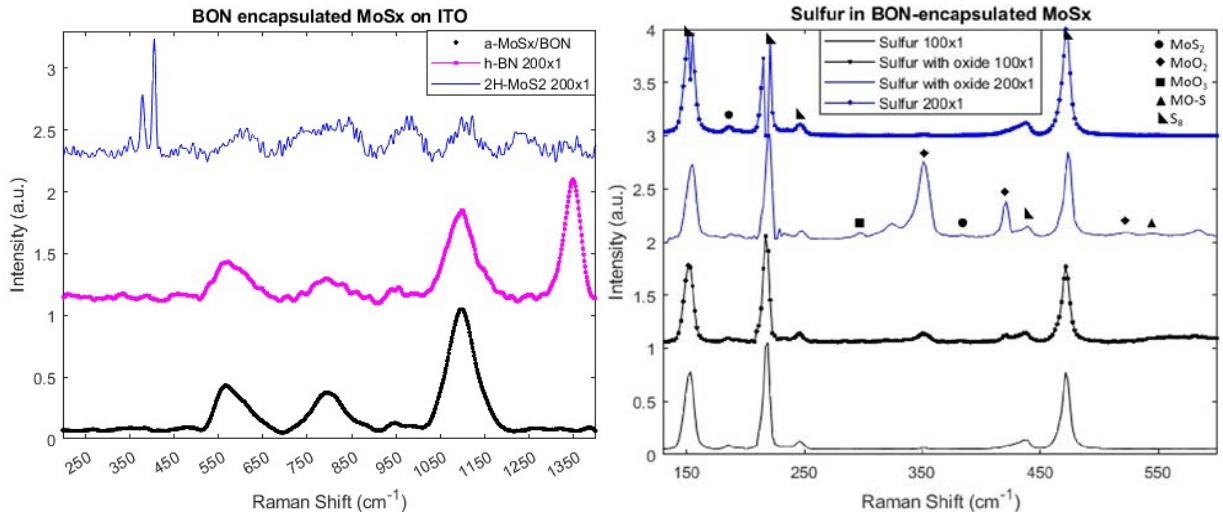

Figure 3.24: **Raman spectra of vibrational modes of MoS_{2+} sample films on ITO-coated glass encapsulated by amorphous BON after being laser annealed at one pulse at beam energies of 100 and 200 mJ.**

At 300 mJ and higher fluences, the films had shown ablation/delamination as pictured in Figure 3.25 and no 2H-MoS_2 was detected.

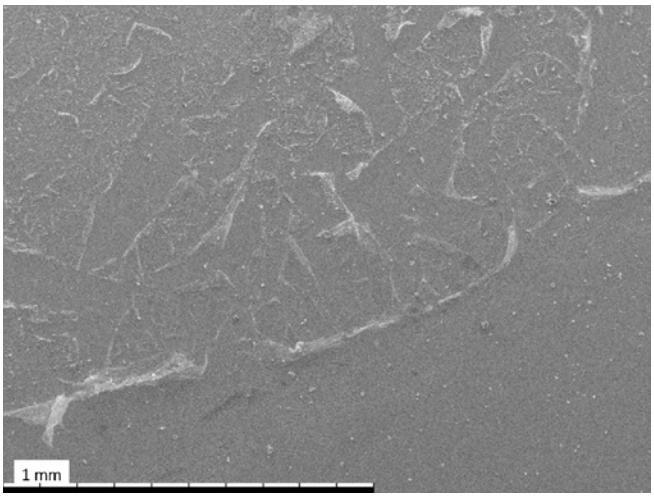

Figure 3.25: **SEM image of amorphous BON after being ablated/delaminated after one pulse of 450 mJ.**

Amorphous BON displays an average optical absorption of 80% at 248 nm with a band gap of 5.4 eV[111] so the BON likely is the cause for the delamination rather than the lower MoS_x or ITO layers. It is unclear if this process for BON was physical (i.e. delamination caused by

thermally induced stress) or chemical (photons rupturing bonds), and whether either are thickness dependent and the BON is too thick at 200-250 nm.

Table 3.19: **Raman peak locations of MoS_x films on encapsulated in amorphous BON after laser annealing.**

Raman Modes	200x1	x-MoS_2	px-MoS_2
E12g	389	386	380
A1g	406	408	405.5

The best quality 2H-MoS_2 films were formed at one pulse at fluence of 200 mJ based on Table 3.19. The films oxidized at one pulse for both 100 and 200 mJ despite the films being sandwiched between 150nm thick ITO and 200-250nm thick amorphous BON. It is unlikely that the films oxidized as a result of oxidation diffusion through the thick amorphous BON as the amorphous structure acts as a diffusion barrier. Instead, the oxygen diffusion from the ITO and BON interfaces are likely the source of oxygen in these laser annealed films. Amorphous BON underwent a phase transformation to form h-BN at both 100 and 200 mJ after one pulse and this process could also release oxygen that leads to the oxidation of MoS_x. The amount of elemental sulfur detected in the encapsulated films is greater than that detected with any other film/substrate combination investigated, which corroborates the theory that the BON prevents sulfur evaporation during phase formation from sulfur rich MoS_x to 2H-MoS_2, but it does not prevent the sulfur from phase segregating into a crystalline form.

3.3.5 Annealing of MoS_x Films on BON/ITO Heterostructures

MIS structures were formed by depositing amorphous BON on ITO-coated glass, followed by depositing amorphous MoS_x precursor to be transformed into semiconducting 2H phase. The films on the BON/ITO heterostructure were annealed at 450 mJ for one, five, and

ten pulses. At one pulse the MoS_x film contained mostly 2H-MoS_2 and a small amount of mixed phase 2H-MoS_2 and MoO_2. At five pulses the films still contain 2H-MoS_2, an equal amount of mixed phase oxide, but now shows a spectrum with MoO_3. The sample still has 2H-MoS_2 after ten pulses but now is mostly a mixed phase 2H-MoS_2 and MoO_2. The amorphous BON layer undergoes a phase transition at five and ten pulses at 450 mJ as evidenced from the h-BN peak at 1350 cm^{-1} shown in Figure 3.26.

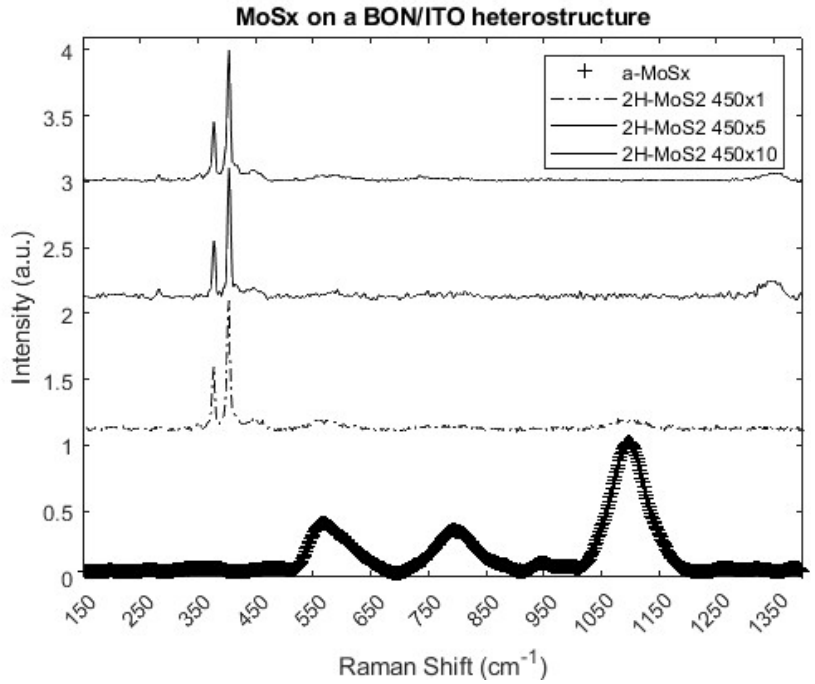

Figure 3.26: **Raman spectra of vibrational modes of MoS_{2+} sample films on a BON-ITO heterostructure stack after being laser annealed at 450 mJ for one, five, and ten pulses.**

Table 3.20: **Raman peak locations of MoSx films on BON/ITO heterostructure stack after laser annealing.**

Raman Modes	450x1	450x5	450x10
E12g	378	378	
A1g	404	404	

No real trend in terms of crystallinity of the films in Table 3.20 was detected as all films exhibited a worse degree of crystallinity than the poorly crystalline samples of 2H-MoS_2

reported in C.H. Chang et al. based on peak location. A clear increase in the oxidation of the films occurred at higher pulse numbers for annealing these MIS structures, where the MoO_2 was the minority phase at one pulse and a near equal amount of MoO_2 and 2H-MoS_2 was present in a mixed phase at ten pulses. The BON/ITO heterostructures were the only substrate in which the MoS_x films were not ablated after annealing at a fluence at 450 mJ for ten pulses.

3.3.6 Annealing of MoS_x Films on Bare Glass Substrates

MoS_x films were deposited on bare glass substrates as they are electrically insulating and could thus be used for Hall effect measurements. MoS_x shown crystallizations of the 2H-MoS_2 phase only when annealed at the highest fluence of 450 mJ for one and five pulses as shown in Figure 3.27. The films were ablated from the substrates after ten pulses for the max fluence allowed.

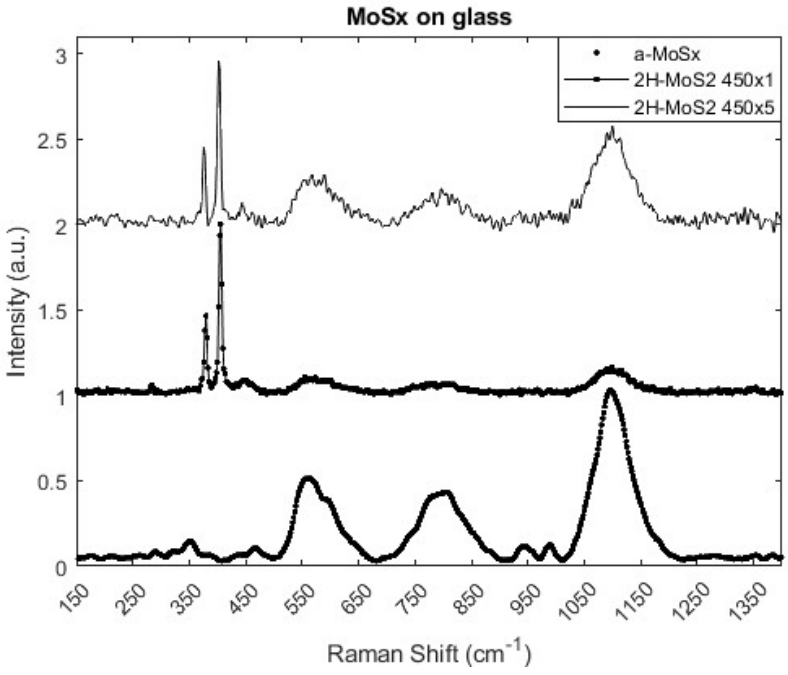

Figure 3.27: **Raman spectra of vibrational modes of MoS_{2+} sample films on bare glass after being laser annealed at 450 mJ for one and five pulses.**

Table 3.21: **Raman peak locations of MoSx films on glass substrates after laser annealing.**

Raman Modes	450x1	450x5	x-MoS_2	px-MoS_2
E12g	379	376	386	380
A1g	406	402	408	405.5

Previously the MoS_x films on glass had not met the crystallization threshold during laser annealing due to the thermal properties of glass, such as low thermal conductivity of 1.05 W/(m-K) and high specific heat of 840 J/(g-K). After a laser refill which allowed the maximum fluence available on our laser system, the films were annealed at 450 mJ which was sufficient to crystallize the films. After one pulse the MoS_x films on glass contained poorly crystalline 2H-MoS_2, and after five pulses the crystallinity decreased as shown in Table 3.21.

3.3.7 Annealing of MoS_x Films on BON-Coated Glass Substrates

Amorphous BON had previously been used as a full encapsulant above and below TMD films, and due to the difficulty annealing on glass the BON was deposited as an interlayer in an attempt to decrease the crystallization threshold towards 2H-MoS_2 crystallization from the difference in thermal properties between glass and BON. MoS_3 deposited on BON-glass was annealed at 450 mJ for one, five, and ten pulses. At one pulse the surface of the film is ruptured from delamination of the BON from glass. However, there are flakes still on the surface that allowed analysis of the MoS_x film which is solely composed of 2H-MoS_2. After five pulses more delamination of BON occurs, and a smaller portion of the total film remains, but still is crystalline 2H-MoS_2 as shown in Figure 3.28. After ten pulses all film is ablated.

The implementation of BON on glass did not lower the crystallization threshold, and instead the MoS_x films crystallized at beam energies of 450 mJ at one and five pulses and was

ablated at ten pulses, where the MoS_x on glass had the same outcomes at the same laser annealing parameters. The only slight deviations between laser annealing of MoS_x films on glass and BON-coated glass were a total lack of oxidation for films on BON-coated glass and the high crystallinity of the 2H-MoS_2 on BON at a single pulse of 450 mJ shown in Table 3.22. The lack of oxidation is presumed to be better adhesion between MoS_x and BON than MoS_x and glass, leading to less sulfur evaporation and infiltration by oxygen.

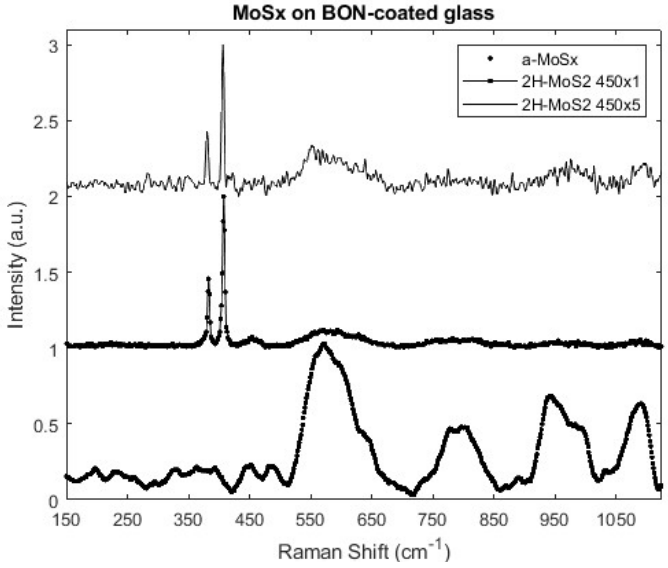

Figure 3.28: Raman spectra of vibrational modes of MoS_{2+} sample films on BON-coated glass after being laser annealed at 450 mJ for one and five pulses.

Table 3.22: **Raman peak locations of MoS_x films on BON-coated glass substrates after laser annealing.**

Raman Modes	450x1	450x5	x-MoS_2	px-MoS_2
E12g	383	380	386	380
A1g	408	407	408	405.5

3.3.8 Annealing of MoS_x Films on SiO_2 Substrates

Thermally grown silicon dioxide has both necessary conditions of favorable thermal properties towards crystallization while being electrically insulating for identifying the films

semiconducting electrical properties through Hall effect measurements. Silicon and SiO_2 have the most beneficial thermal properties of all substrates used in this work, such as thermal conductivity of 148 and 1.3 W/m K and specific heat, for silicon and SiO_2, respectively. Therefore, the MoS_x films on SiO_2 underwent the most thorough laser annealing from 100, 200, 300, 400, and 450 mJ one for one, five, and ten pulses.

The samples annealed at 100 mJ for one pulse yeilded a high crystalline quality 2H-MoS_2 regions (these have high intensity and narrow FWHM characteristic Raman peaks) as well as regions with mixed phases of 2H-MoS_2 and MoO_2. After five pulses no 2H-MoS_2 remained but there was some MoO_3, and ten pulses resulted in a complete ablation. One pulse of the MoS_x film at a fluence of 200 mJ also generates a good crystalline quality 2H-MoS_2 with a small portion of MoO_3 and mixed phase MoO_2 and 2H-MoS_2. After five pulses the amount and quality of 2H-MoS_2 crystallites was unchanged but no oxides were detected. After ten pulses at 200 mJ, elemental sulfur phase is formed and both MoO_2 and MoO_3 are present at the surface.

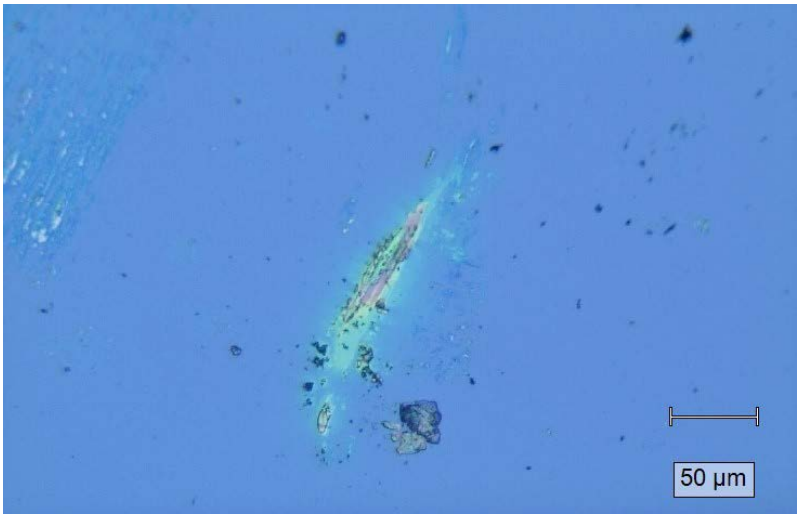

Figure 3.29: **Optical images of sulfur-rich site of MoS_{2+} on SiO_2 substrate after being laser annealed at 300 mJ for one pulse.**

For MoS_x films annealed at 300 mJ, one pulse induces 2H-MoS_2 phase as well as the

elemental sulfur segregation shown in Figure 3.29 with a small fraction of oxide growth. After five pulses at 300 mJ, the poorly crystalline 2H phase is present with the same amount of oxide, and no more elemental sulfur is detected. After ten pulses only MoO_3 remains with signs of the film ablation. MoS_x annealed at 400 mJ for one pulse promoted mostly MoO_2 formation with only one spectrum of 2H-MoS_2 detected with a small amount of mixed phase oxide as shown in Figure 3.30 (right). After five pulses the 2H phase grows and increases in crystallinity, with a reduction in the relative fraction of oxide phase. After ten pulses the elemental sulfur segregates, while the 2H phase continues to grow in phase fraction and increases in crystallinity, with the relative fraction of oxide reducing even more. For MoS_x annealed at a maximum fluence of 450 mJ for one pulse, Raman analysis detected mostly poorly crystalline 2H-MoS_2 with a small amount of MoO_3. After five pulses there is very little film present at the surface due to ablation with only a single flake of MoO_3 detected. Finally, at ten pulses of 450 mJ no films remain on the surface.

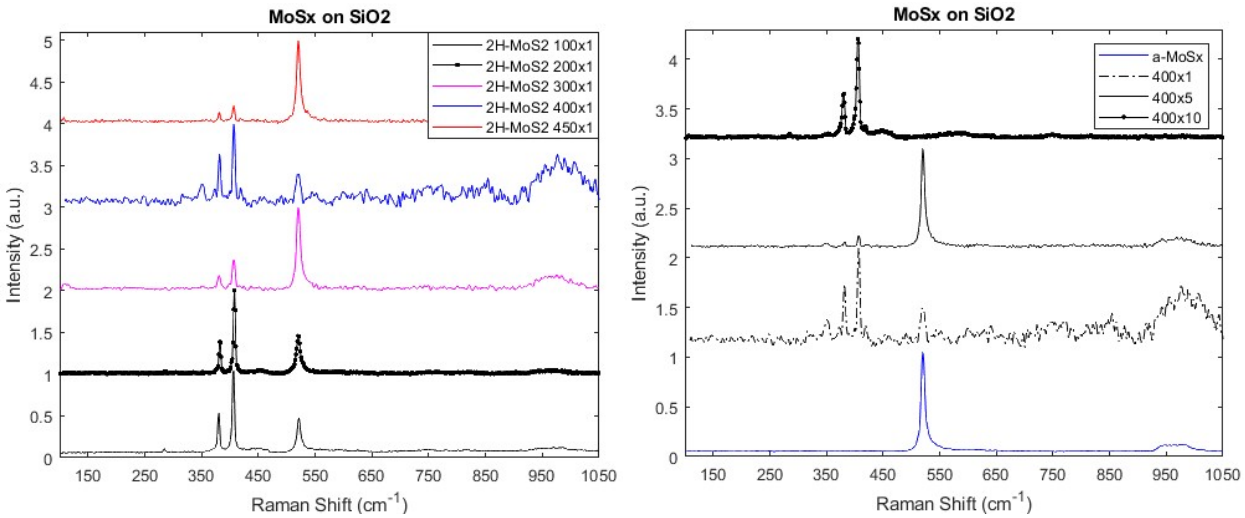

Figure 3.30: **Raman spectra of vibrational modes of MoS_x sample films on SiO_2 after being laser annealed for one pulse at beam energies of 100, 200, 300, 400, and 450 mJ (left) and one, five, and ten pulses at 400 mJ (right).**

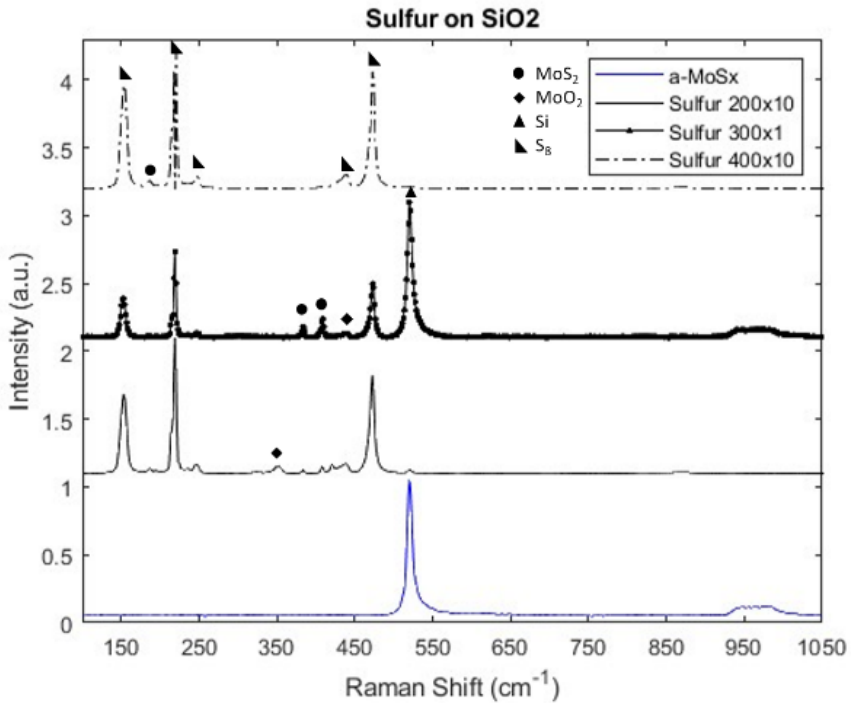

Figure 3.31: **Raman spectra of vibrational modes of MoS_x sample films on SiO_2 which contain sulfur crystallites after being laser annealed for ten pulses at 200 mJ, one pulse at 300 mJ, and ten pulses at 400 mJ.**

These thermal properties reduced the threshold towards crystallization as MoS_x films on SiO_2 underwent the phase transformation to 2H-MoS_2 on SiO_2 at the lowest fluence and number of pulses possible for our laser system (one pulse at 100 mJ) and the lowest for all substrates in this study. Further, the MoS_3 films suffered the least amount of ablation on SiO_2 vs. all other substrates. All films on SiO_2 formed 2H-MoS_2 for one pulse for all fluences as shown in Figure 3.31.

Based on Table 3.23, the SiO_2 the films tended to be best after a single pulse, where only one fluence of 400 mJ promoted growth in 2H-MoS_2 and better film quality at a higher number of pulses. The films with the highest crystallinity on SiO_2 were annealed at a fluence of 200 mJ while higher fluences of 400 and 450 mJ promoted more growth of the 2H phase, leading to the only network of 2H-MoS_2 forming at 450 mJ.

Table 3.23: **Raman peak locations of MoS_x films on SiO_2 after laser annealing.**

Raman Modes	100x1	200x1	200x5	300x1	300x5	400x1	400x5	400x10	450x1
E12g	380	382	382	380	383	382	382	380	382
A1g	407	408	408	406	408	407	407	405	404

3.3.9 Summary of Laser Annealing of Films on Various Substrates

Raman analysis confirmed all substrates were covered by an amorphous film before annealing, and 2H-MoS_2 was formed on every investigated substrate surface except for the BON-coated SiO_2 surface. MoS_x on every substrate besides films on ITO-coated glass and encapsulated BON on ITO-coated glass were confirmed to be ultra-thin based on a broad feature composed of three peaks at 440, 450, 459 cm^{-1} which forms for ultra-thin 2H-MoS_2.[34, 88]

Overall, a critical threshhold fluence of the laser energy was always necessitated in order to reach a phase transformation. MoS_x films on ITO-coated glass were the only films where 2H-MoS_2 was not formed after one pulse of a given fluence, but a higher number of pulses at the same fluence was sufficient for crystallizing 2H-MoS_2. All other film/substrate combinations that did not induce crystallization for a given fluence at one pulse was also unsuccessful in yielding crystallization at the same fluence for a larger number of pulses. Instead, increasing fluence to meet the critical fluence threshold was necessary in order to reach a phase transformation. As a general observation across all substrates, a lower number of pulses at a given critical fluence was needed to induce crystallization with a more pronounced formation of 2H-MoS_2 phase as compared to oxide phase formation. Counterintuitively, for a given fluence that is above the critical for crystallization, the best 2H-MoS_2 crystallinity was

observed at a single pulse for all substrates. If 2H-MoS_2 formed at a lower number of pulses for a given fluence, a higher number of pulses at that same fluence resulted in a reduction in crystallinity of the 2H phase and the increase in oxide formation.

The decomposition at higher number of pulses is evidenced by the segregation of sulfur and the formation of elemental sulfur that formed for MoS_x films on SiO2 and films encapsulated by BON after laser annealing at higher fluences, where the decomposition of 2H-MoS_2 is likely caused by the evaporation of sulfur at higher temperatures induced from laser irradiation. There is also a thermodynamic competition of 2H-MoS_2, m-MoO_2, and α-MoO_3, where m-MoO_2 and α-MoO_3 form at higher temperatures.[35] Mixed phases of 2H-MoS_2 and evidence of MoO_2 and/or MoO_3 were also formed for all substrates after laser annealing. Higher number of pulses generally led to an increase in the fraction of oxides detected. There was a transition of MoS_x to MoO_2 evidenced by the mixed 2H-MoS_2 and MoO_2 phase present for all substrate types, then a slow transition of m-MoO_2 to α-MoO_3 at higher number of pulses and fluences.[35] C.H. Change et al. and Lince et al. both report MoS_3 films decomposing into MoO_3 at higher laser powers, where excessive heating MoS_3 from laser irradiation in ambient environments caused the oxidation.[75-76]

Only films deposited on SiO_2 or encapsulated by BON formed elemental sulfur phases. This was assumed to be due to the decomposition of amorphous MoS_3 to crystalline MoS_2 where the reaction is proposed by Lince et al. to be,

$$MoS_3 \rightarrow MoS_2 + \text{crystalline S}$$

which occurs at temperatures above 350 °C.[61], [76] The sulfur crystals were confirmed to be the γ-S8 crystal structure from the respective vibrational modes during Raman analysis. Thus, the

presence of elemental sulfur is evidence of MoS_3 precursor on those substrates which decomposed after laser irradiation. Sulfur crystallized for MoS_x films on SiO_2 at higher fluences. likely indicating the laser irradiation necessary to heat the films to 350 °C, and contained a mixed phase of MoS_2 and α-S8, as predicted by the proposed decomposition reaction. The 2H-MoS_2 with the highest crystallinity based on peak location was measured in this study were found in the sulfur phases on the SiO_2 substrate produced from 200 mJ at ten pulses and 300 mJ at a single pulse. After 400 mJ at ten pulses, the 2H-MoS_2 in sulfur displays very short broad peaks that are easily missed shown in Figure 3.32. This is likely an indicator that the decomposition of amorphous MoS_3 into 2H-MoS_2 and α-S has been exhausted, which could explain why the following sets of samples annealed at 450 mJ at one pulse formed the only continuous network of 2H-MoS_2. More sulfur crystallites formed from the laser annealing of MoS_x encapsulated by BON than any other samples, yet the 2H-MoS_2 peaks in the sulfur crystallites are similarly broad with low intensities as shown in Figure 3.24. Instead, oxides formed likely as a result of the phase transition of amorphous BON to h-BN which took place and released oxygen.

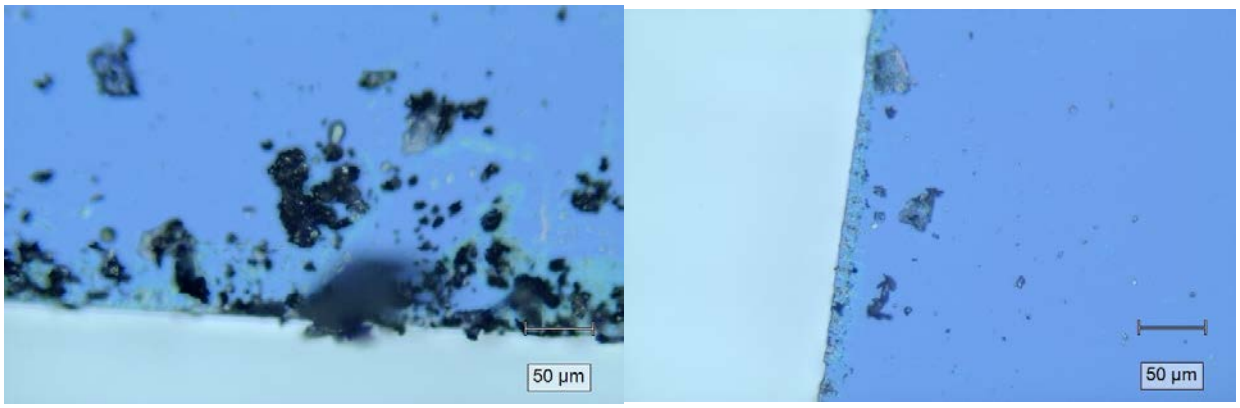

Figure 3.32: **Optical images of MoS_{2+} crystallites on edge of SiO_2 substrate after being laser annealed for five pulses at 400 mJ (left) and one pulse at 450 mJ (right).**

All substrate types yield some amount of ablation and/or delamination at the high fluences during amorphous MoS_x film annealing. A higher number of pulses generally led to ablation, where only the films on the MIS structure was not ablated at 450 mJ for 10 pulses. All other films were annealed at 450 mJ for high numbers of pulses or were ablated at lower temperatures. Ablation likely was likely most dependent on film adhesion to the substrate, as films on substrates with different thermal properties did not fair any differently at the maximum fluence. Amorphous BON was used as an interlayer and encapsulant in order to reduce ablation and oxidation from better adhesion and protecting the MoS_x from ambient environment. BON as an encapsulant did not prevent oxidation, as the MoS_x film may have oxidized from the oxygen in BON after sputtering, but the BON seemed to prevent sulfur evaporation evidenced by the amount of elemental sulfur at later fluences. BON as an interlayer did allow the highest fluence and number of pulses combo where all other films ablated, which also limited the oxidation of the films. Hexagonal BN formed for both the encapsulated film and MIS structure, while it could not be determined if the amorphous BON on glass formed h-BN as it had some amount of ablation/delamination for all number of pulses.

3.4 Electronic Properties of the Films

Electrically insulating substrates are required to record Hall effect measurements of the films, so although films on glass ITO-coated glass had promising homogeneity of 2H-phase and high conductivity, they are incompatible with Hall measurements to record the film's carrier type which was the motivation for depositing insulating BON layers on top of it. However, the MoS_x films annealed on the MIS did not display the level of crystallinity necessary, and the MoSx films deposited and annealed on SiO2 substrates were selected for Hall effect

measurements. Films on SiO2 were only films that grew in 2H phase at higher fluences, where a network of 2H-MoS_2 formed along the edges of the SiO_2 after annealing at 400 mJ for five pulses and at 450 mJ for one pulse, as shown in Figure 3.32.

Ultimately the 2H phase formed at 450 mJ for one pulse displays the conductivity required for Hall measurements, where the results can be seen in Table 3.24. Films were expectedly p-type as a result of the excess-sulfur, with high bulk and sheet concentrations, respectable conductivity, and high mobility.

Table 3.24: **Hall effect measurements of p-type MoS_{2+} on SiO_2 after laser annealing at 450mJ energy for one pulse.**

Test number	Bulk Concentration [/cm³]	Sheet Concentration [/cm2]	Resistivity [Ω-cm]	Conductivity [1/Ω-cm]	Magneto-Resistance [Ω]	Mobility [cm²/Vs]	Average Hall Coefficient [cm³/C]
1	-3.50E+19	-7.00E+13	2.44E-05	4.10E+04	2.67E+04	7.31E+03	-1.78E-01
2	1.55E+17	3.10E+11	2.73E-05	3.67E+04	1.65E+04	1.48E+06	4.02E+01
3	3.67E+16	7.34E+10	2.79E-02	3.58E+01	3.12E+04	6.10E+03	1.70E+02
4	2.06E+17	4.11E+11	9.89E+01	1.01E-02	4.74E+04	3.07E-01	3.04E+01
5	1.34E+18	2.67E+12	6.95E-04	1.44E+03	4.15E+04	6.73E+03	4.67E+00
P-type average	4.33E+17	8.66E+11	2.47E+01	9.53E+03	3.41E+04	3.72E+05	6.14E+01

CHAPTER 4

CONCLUSIONS

The original scientific hypothesis for the ability to produce p-type crystalline TMD films by laser annealing of sulfur-rich amorphous precursor films produced by magnetron sputtering from targets with high chalcogenide content has been confirmed. Several knowledge gaps important to the scientific and engineering community regarding TMD thin films were filled by the results of this study; including how excess-chalcogen TMD sputtering targets can be produced, how they perform over extended sputtering time, and how the growth of amorphous chalcogen-rich precursors at room temperature can be accomplished and coupled with laser annealing for conversion to crystalline 2H phases to produce p-type semiconducting TMD films.

It was found that the ball milling and hotpressing processing methods proved to be the best manufacturing techniques for producing highly crystalline denser targets with the highest chalcogen to transition metal ratio in the range of 2.7-4.2 for W-S, Mo-S and W-Se sputtering targets . Acoustic mixing and liquid phase sintering were found to provide good target homogeneity and reduced sulfur phase segregation, but the acoustic mixing added more oxygen to the powder than ball milling. The oxygen incorporation can be reduced by using a vacuum processing environment, the porosity of the liquid phase sintered targets limits its current usability and needs to be addressed with changes in processing parameters. Based on these results, sulfur-rich $WS_{2.7}$ and $MoS_{3.6}$ targets prepared by ball milling and hotpressing were selected for the studies of TMD film sputtering and laser annealing.

The excess-sulfur targets prepared by ball milling and hotpressing performed well during

sputtering. The decrease of sulfur to metal ratio during sputtering was analyzed from the perspective of the target surface and bulk evolution over extended periods of sputtering using $WS_{2.7}$ target as a representative example. A decrease in S:W ratio was found over extended sputtering use for both the excess-sulfur and stoichiometric targets. The determined mechanism was the selective sputtering of sulfur, leading to surface depressions and the formation of metal dendrite structure in such sulfur depleted regions. An observation was also made for additional elemental sulfur phase segregation in the presence of metal dendrites. It was hypothesized to be caused by a process similar to that of sulfur electrodes in batteries and where the tungsten was concluded to act as a catalyst. This suggested mechanism was corroborated by SEM/EDX, Raman, XRD and XPS results. Polishing target surfaces proved to be a necessary maintenance step for all TMD based targets used in this work, where polishing both removed damage and restored, and in some cases improved, the chalcogen to transition metal ratio of the targets.

The amorphous sulfur-rich TMD precursor films were produced at the room temperature by sputtering a $MoS_{3.6}$ target. MoS_x films (with x in the range of 2.4-2.6) were deposited at a working pressure of 10 and 20 mTorr and contained a ratio of MoS_2 and MoS_3 compounds. These precursor films sputtered at a working pressure of 20 mTorr yield a higher S:W ratio and were the only films which provided 2H-MoS_2 crystallization after laser annealing at 100 mJ for ten pulses. From these results, a working pressure of 20 mTorr was selected for succeeding sulfur-rich TMD film synthesis.

Produced sulfur rich precursor MoS_x films were successfully crystallized by laser annealing with 248 nm laser beam in air on all substrate types used in this study (BON, ITO,

glass, SiO_2) and confirmed to be ultra-thin by way of Raman analysis. For the considered substrates, the highest crystalline quality films were found to form when using the lowest number of pulses with fluences exceeding the threshold of the crystallization. The crystallization threshold was dependent on the used substrates, ranging from 100 mJ for films on SiO_2 to 450 mJ for films on glass. Increasing fluences above threshold and increasing number of pulses led to preferential growth of molybdenum oxides rather than the 2H-MoS_2 phase, which was a competing phase formation mechanism during the laser annealing in air. MoSx films on SiO_2 and ITO-coated glass had the lowest threshold for crystallization at 100 mJ and produced the films of highest crystallinity of the 2H-MoS_2 phase.

A network of 2H-MoS_2 crystals on SiO2 was formed for MoS_x films laser annealed on SiO_2 at 450 mJ fluence for a single pulse, allowing Hall effect measurements to be recorded. The 2H-MoS_2 film was confirmed to be p-type based on the bulk and sheet concentration of holes of 4.33E+17/cm^3 and 8.66E+11/cm^2 , respectively. The films had a modest conductivity of 9.53E+03/Ω-cm and a high mobility of 3.72E+05 cm^2/Vs. Hall effect measurements confirmed sulfur-rich is p-type with electrical properties which are favorable for use in optoelectronics, which validates the approach of coupling the room temperature sputtering with excess-sulfur targets and laser annealing the sulfur-rich amorphous precursors into p-type 2H-MoS_2 semiconducting films.

The results of this work clearly demonstrate that the suggested preparation of sulfur-rich targets and coupling of RF magnetron sputtering and UV laser annealing processes allow for the room temperature sputtering of amorphous TMD precursors and their laser annealing to 2H crystalline phases universally on multiple substrate types. Furthermore, the suggested

process can produce films as n- or p-type based on either changes in magnetron sputtering deposition parameters or laser annealing parameters for controlling the S:W ratio of the films. This allows for the formation of P/N junctions or heterojunctions of TMDs on polymers or other substrates without the added steps of a transfer method, doping, or an additional sulfur incorporation by a high temperature annealing. This permits high throughput and scalable production of electronic devices, such as transistors, sensors, photodetectors, or photovoltaics on variety of substrates.

CHAPTER 5

FUTURE WORK

5.1 Target Manufacturing

Liquid phase sintering was promising in making homogenous targets with low amounts of oxygen inclusions, but the processing parameters need to be fine-tuned in order to decrease their porosity and limit the evaporation of the chalcogen atoms during sintering.

5.2 Sputtering Use of Chalcogen-Rich Targets

Further testing is needed for other TMDs targets to determine if the chalcogen-deficiencies found in the W-S targets are common across TMDs after sputtering use. Likewise, targets composed of binary compounds with large differences in vapor pressure must be tested to determine if this phenomenon is not exclusive to WS_2 or other TMDs.

5.3 Laser Annealing

The sulfur-rich MoS_x were annealed on different substrate at the maximum fluences allowed with the laser used in this work. Using higher fluences or employing rastering may be required to produce more continuous 2H-films. Additionally, since this manufacturing processing is acceptable of polymer substrates, depositing MoS_x films and annealing directly on polymer substrates needs to be tested. Full device implantation of either transistors or devices with heterojunctions could be manufactured using n- and p-type films deposited from the same excess-sulfur target and laser annealed is now possible.

REFERENCES

1. U.S. Department of Energy Solar Energy Technologies Office. 2021. Solar Energy Technologies Office Updated 2030 Goals for Utility-Scale Photovoltaics. Retrieved from https://www.energy.gov/articles/doe-announces-goal-cut-solar-costs-more-half-2030

2. Woodhouse, Michael, Rebecca Jones-Albertus, David Feldman, Ran Fu, Kelsey Horowitz, Donald Chung, Dirk Jordan, and Sarah Kurtz. 2016. On the Path to SunShot: The Role of Advancements in Solar Photovoltaic Efficiency, Reliability, and Costs. Golden, CO: National Renewable Energy Laboratory. NREL/TP-6A20-65872. http://www.nrel.gov/docs/fy16osti/65872.pdf.

3. U.S. Energy Information Administration. 2021. Annual Energy Outlook 2021 (AEO2021) Assumptions document (Cost and Performance Characteristics of New Generating Technologies). Retrieved from https://www.eia.gov/outlooks/aeo/assumptions/pdf/table_8.2.pdf

4. N. R. Glavin, C. Muratore, and M. Snure, “Toward 2D materials for flexible electronics: opportunities and outlook,” Oxf. Open Mater. Sci., vol. 1, no. 1, p. itaa002, Nov. 2020, doi: 10.1093/oxfmat/itaa002

5. C. W. Lee, J. M. Suh, and H. W. Jang, “Chemical Sensors Based on Two-Dimensional (2D) Materials for Selective Detection of Ions and Molecules in Liquid,” Front. Chem., vol. 7, p. 708, Nov. 2019, doi: 10.3389/fchem.2019.00708.

6. P. Feng, E. Chavez, and C. Malca, “Super Stable Pollution Gas Sensor Based on Functionalized 2D Boron Nitride Nanosheet Materials for High Humidity Environments,” Chemosensors, vol. 6, no. 4, p. 49, Nov. 2018, doi: 10.3390/chemosensors6040049.

7. G. Wang et al., “Two dimensional materials based photodetectors,” Infrared Phys. Technol., vol. 88, pp. 149–173, Jan. 2018, doi: 10.1016/j.infrared.2017.11.009.

8. Y. Xue et al., “Scalable Production of a Few-Layer MoS 2 /WS 2 Vertical Heterojunction Array and Its Application for Photodetectors,” ACS Nano, vol. 10, no. 1, pp. 573–580, Jan. 2016, doi: 10.1021/acsnano.5b05596.

9. B. Sirota, N. Glavin, S. Krylyuk, A. V. Davydov, and A. A. Voevodin, “Hexagonal MoTe2 with Amorphous BN Passivation Layer for Improved Oxidation Resistance and Endurance of 2D Field Effect Transistors,” Sci. Rep., vol. 8, no. 1, p. 8668, Dec. 2018, doi: 10.1038/s41598-018-26751-4.

10. M. A. Uddin et al., “Mobility enhancement in graphene transistors on low temperature pulsed laser deposited boron nitride,” Appl. Phys. Lett., vol. 107, no. 20, p. 203110, Nov. 2015, doi: 10.1063/1.4936191.

11. Benjamin Sirota, Nicholas Glavin, Andrey A. Voevodin, Room temperature magnetron sputtering and laser annealing of ultrathin MoS2 for flexible transistors, Vacuum, Volume 160, 2019, Pages 133-138, ISSN 0042-207X, https://doi.org/10.1016/j.vacuum.2018.10.077.

12. Bhandavat, Romil & David, Lamuel & Singh, Gavrav. (2012). Synthesis of Surface-Functionalized WS2 Nanosheets and Performance as Li-Ion Battery Anodes. The Journal of Physical Chemistry Letters. 3. 1523-1530. 10.1021/jz300480w.

13. E. Cha, D. K. Kim, and W. Choi, "Advances of 2D MoS2 for High-Energy Lithium Metal Batteries," Front. Energy Res., vol. 9, p. 645403, Mar. 2021, doi: 10.3389/fenrg.2021.645403.

14. R. Rojaee and R. Shahbazian-Yassar, "Two-Dimensional Materials to Address the Lithium Battery Challenges," ACS Nano, vol. 14, no. 3, pp. 2628–2658, Mar. 2020, doi: 10.1021/acsnano.9b08396.

15. Konstantatos, G., Badioli, M., Gaudreau, L. *et al.* Hybrid graphene–quantum dot phototransistors with ultrahigh gain. *Nature Nanotech* **7,** 363–368 (2012). https://doi.org/10.1038/nnano.2012.60

16. L. Zeng et al., "High-responsivity UV-Vis Photodetector Based on Transferable WS2 Film Deposited by Magnetron Sputtering," Sci. Rep., vol. 6, no. 1, p. 20343, Apr. 2016, doi: 10.1038/srep20343.

17. Ong, Sean, Clinton Campbell, Paul Denholm, Robert Margolis, and Garvin Heath. 2013. Land-Use Requirements for Solar Power Plants in the United States. Golden, CO: National Renewable Energy Laboratory. NREL/TP-6A20-56290 https://www.nrel.gov/docs/fy13osti/56290.pdf.

18. Gagnon, Pieter, Robert Margolis, Jennifer Melius, Caleb Phillips, and Ryan Elmore. 2016. Rooftop Solar Photovoltaic Technical Potential in the United States: A Detailed Assessment. Golden, CO: National Renewable Energy Laboratory. NREL/TP-6A20-65298. https://www.nrel.gov/docs/fy16osti/65298.pdf.

19. Z. Ahmadi, P. Fathi-Hafshejani, E. Kayali, M. Beidaghi, and M. Mahjouri-Samani, "Rapid laser nanomanufacturing and direct patterning of 2D materials on flexible substrates—2DFlex," Nanotechnology, vol. 32, no. 5, p. 055302, Jan. 2021, doi: 10.1088/1361-6528/abc285.

20. M. Zou, Y. Ma, X. Yuan, Y. Hu, J. Liu, and Z. Jin, "Flexible devices: from materials, architectures to applications," J. Semicond., vol. 39, no. 1, p. 011010, Jan. 2018, doi: 10.1088/1674-4926/39/1/011010

21. D. Akinwande, N. Petrone, and J. Hone, "Two-dimensional flexible nanoelectronics," Nat. Commun., vol. 5, no. 1, p. 5678, Dec. 2014, doi: 10.1038/ncomms6678.

22. R. H. Rai, A. Pérez-Pacheco, R. Quispe-Siccha, N. R. Glavin, and C. Muratore, “Pulsed laser annealing of amorphous two-dimensional transition metal dichalcogenides,” J. Vac. Sci. Technol. A, vol. 38, no. 5, p. 052201, Sep. 2020, doi: 10.1116/6.0000253.

23. M. E. McConney et al., “Direct synthesis of ultra-thin large area transition metal dichalcogenides and their heterostructures on stretchable polymer surfaces,” J. Mater. Res., vol. 31, no. 7, pp. 967–974, Apr. 2016, doi: 10.1557/jmr.2016.36.

24. H. Wang, S.M. Ng, H.F. Wong, W.C. Wong, K.K. Lam, Y.K. Liu, L.F. Fei, Y.B. Zhou, C.L. Mak, Y. Wang, C.W. Leung. Effect of post-annealing on laser-ablation deposited WS2 thin films, Vacuum, Volume 152, 2018, Pages 239-242, ISSN 0042-207X, https://doi.org/10.1016/j.vacuum.2018.03.024.

25. Adam R. Waite, Shanee Pacley, Nicholas R. Glavin, Andrey A. Voevodin, Christopher Muratore,

26. G.Y. Du, D.C. Ba, Z. Tan, K. Liu, Research on Frictional Behavior of Tungsten Disulfide Thin Films Prepared by Rf Magnetron Sputtering on Restless Steel, Physics Procedia, Volume 32, 2012, Pages 532-538, ISSN 1875-3892, https://doi.org/10.1016/j.phpro.2012.03.597.

27. Phys.Chem.Chem.Phys., 2014, 16, 1008

28. R. H. Kim et al., “Photonic Crystallization of Two-dimensional MoS2 for Stretchable Photodetectors,” p. 25.

29. Guangxing Liang, Xingye Chen, Rong Tang, Yike Liu, Yingfen Li, Ping Luo, Zhenghua Su, Xianghua Zhang, Ping Fan, Shuo Chen, Spark plasma sintering of Sb2Se3 sputtering target towards highly efficient thin film solar cells, Solar Energy Materials and Solar Cells, Volume 211, 2020, 110530, ISSN 0927-0248, https://doi.org/10.1016/j.solmat.2020.110530.

30. K.F. Mak, C. Lee, J. Hone, J. Shan, T.F. Heinz, Atomically thin MoS2 : a new directgap semiconductor, Phys. Rev. Lett. 105 (2010) 136805

31. J. Ren, Y. Zhou, L. Xia, Q. Zheng, J. Liao, E. Long, F. Xie, C. Xu and D. Lin*, J. Mater. Chem. A*, 2018, DOI:10.1039/C8TA04675A.

32. *ACS Appl. Nano Mater.* 2022, 5, 5, 7549–7561 Publication Date:May 10, 2022 https://doi.org/10.1021/acsanm.2c01614

33. Wang et al. Nano Convergence 2014, 1:22 http://www.nanoconvergencejournal.com/content/1/1/22

34. H. Li et al., “From Bulk to Monolayer MoS2: Evolution of Raman Scattering,” Adv. Funct. Mater., vol. 22, no. 7, pp. 1385–1390, Apr. 2012, doi: 10.1002/adfm.201102111.

35. M.A. Camacho-López, L. Escobar-Alarcón, M. Picquart, R. Arroyo, G. Córdoba, E. Haro-Poniatowski, Micro-Raman study of the m-MoO2 to α-MoO3 transformation induced by cw-laser irradiation, Optical Materials, Volume 33, Issue 3, 2011, Pages 480-484, ISSN 0925-3467, https://doi.org/10.1016/j.optmat.2010.10.028.

36. Rathod, U.P., Jha, J.K., Voevodin, A.A. *et al.* A photoelectron study of annealing induced changes to workfunction and majority carrier type in pulsed laser deposited few layer WS_2 films. *J Mater Sci: Mater Electron* **29,** 20051–20056 (2018). https://doi.org/10.1007/s10854-018-0135-5

37. Qiao, Shuai & Yang, Hang & Bai, Zongqi & Peng, Gang & Zhang, Xueao. (2017). Identifying the number of WS2 layers via Raman and photoluminescence spectrum. 10.2991/icmmcce-17.2017.247.

38. Berkdemir, A., Gutiérrez, H., Botello-Méndez, A. et al. Identification of individual and few layers of WS2 using Raman Spectroscopy. Sci Rep 3, 1755 (2013). https://doi.org/10.1038/srep01755

39. Y Q Qin *et al* 2020 *IOP Conf. Ser.: Mater. Sci. Eng.* **770** 012079

40. Hotovy, L. Spiess, M. Mikolasek, I. Kostic, H. Romanus, Structural and morphological evaluation of layered WS2 thin films, Vacuum, Volume 179, 2020, 109570, ISSN 0042-207X, https://doi.org/10.1016/j.vacuum.2020.109570.

41. Tan SM, Pumera M. Bottom-up Electrosynthesis of Highly Active Tungsten Sulfide (WS3-x) Films for Hydrogen Evolution. ACS Appl Mater Interfaces. 2016 Feb 17;8(6):3948-57. doi: 10.1021/acsami.5b11109. Epub 2016 Feb 4. PMID: 26844594.

42. O. Lignier, G. Couturier, J. Salardenne, Growth mechanism of 2H–WS2 thin films: a similar process to graphitization, Thin Solid Films, Volume 338, Issues 1–2, 1999, Pages 75-80, ISSN 0040-6090, https://doi.org/10.1016/S0040-6090(98)00997-3.

43. Yuan-Ron Ma, Chi-Ming Lin, Chun-Liang Yeh, Rong-Tan Huang, "Synthesis and characterization of one-dimensional WO2 nanorods", Journal of Vacuum Science & Technology B: Microelectronics and Nanometer Structures Processing, Measurement, and Phenomena 23, 2141-2145 (2005) https://doi.org/10.1116/1.2050668

44. Jian-Ping Zou, Jun Ma, Jin-Ming Luo, Jian Yu, Junkai He, Yongtao Meng, Zhu Luo, Shao-Kui Bao, Hui-Long Liu, Sheng-Lian Luo, Xu-Biao Luo, Tong-Cai Chen, Steven L. Suib, Fabrication of novel heterostructured few layered WS2-Bi2WO6/Bi3.84W0.16O6.24 composites with enhanced photocatalytic performance, Applied Catalysis B: Environmental, Volume 179, 2015, Pages 220-228, ISSN 0926-3373, https://doi.org/10.1016/j.apcatb.2015.05.031.

45. S. M. Tan, M. Pumera, *Chem. Eur. J.* **2017**, *23*, 8510.

46. Yuvasravan, R., Apsana, G., George, P.P. *et al.* Synthesis of WS_2 and WSe_2 nanowires on stainless steel coupon by reaction under autogenic pressure at elevated temperature method. *Appl Nanosci* **6,** 855–862 (2016). https://doi.org/10.1007/s13204-015-0503-x

47. Wonbong Choi, Nitin Choudhary, Gang Hee Han, Juhong Park, Deji Akinwande, Young Hee Lee, Recent development of two-dimensional transition metal dichalcogenides and their applications, Materials Today, Volume 20, Issue 3, 2017, Pages 116-130, ISSN 1369-7021, https://doi.org/10.1016/j.mattod.2016.10.002.

48. Alam, Tarek; Wang, Baoming; Pulavarthy, Raghu; Haque, M. Amanul; Muratore, Christopher; Glavin, Nicholas R.; Roy, Ajit K.; and Voevodin, Andrey A., "Domain Engineering of Physical Vapor Deposited Two-Dimensional Materials" (2014). *Chemical and Materials Engineering Faculty Publications*. 98.

49. Christopher Muratore, Andrey A. Voevodin, Nicholas R. Glavin, Physical vapor deposition of 2D Van der Waals materials: a review, Thin Solid Films, Volume 688, 2019, 137500, ISSN 0040-6090, https://doi.org/10.1016/j.tsf.2019.137500.

50. Laser Annealing of Semiconductors, edited by J.M. Poate and James W. Mayer

51. Yang, S.T. et al. Applied Optics, Vol. 49, No. 14, 10 (2010)

52. Förster, J., and H. Vogt. “Excimer Laser-Annealing of Amorphous Silicon Layers.” 2011 COMSOL Conference in Stuttgart

53. Urmila P. Rathod, Justin Egede, Andrey A. Voevodin, *and* Nigel D. Shepherd, "Extrinsic p-type doping of few layered WS_2 films with niobium by pulsed laser deposition", Appl. Phys. Lett. 113, 062106 (2018) https://doi.org/10.1063/1.5040119

54. Urmilaben P. Rathod, Bimin Cai, Chukwudi Iheomamere, Gilbert Nyandoto, Andrey A. Voevodin, and Nigel D. Shepherd , "Growth of pulsed laser deposited few-layer WS2 films", Journal of Vacuum Science & Technology A 37, 051505 (2019) https://doi.org/10.1116/1.5111727

55. Andrey A. Voevodin, Adam R. Waite, John E. Bultman, Jianjun Hu, Christopher Muratore, Magnetic field argon ion filtering for pulsed magnetron sputtering growth of two-dimensional MoS2, Surface and Coatings Technology, Volume 280, 2015, Pages 260-267, ISSN 0257-8972, https://doi.org/10.1016/j.surfcoat.2015.09.013.

56. J.G. Jones, A.A. Voevodin, Magnetron sputter pulsed laser deposition: technique and process control developments, Surface and Coatings Technology, Volume 184, Issue 1, 2004, Pages 1-5, ISSN 0257-8972, https://doi.org/10.1016/j.surfcoat.2003.10.016.\

57. *ACS Appl. Mater. Interfaces* 2014, 6, 13, 10408–10414 Publication Date:June 6, 2014 https://doi.org/10.1021/am501940x

58. R.P Elliot, Constitution of Binary Alloys, First Supplement. McGraw-Hill; 1st edition (January 1, 1965)

59. William B. Johnson, A MOLYBDENUM SULFUR BINARY PHASE DIAGRAM Scripta METALLURGICA Vol. 17, pp. 919-922, 1983 Pergamon Press Ltd.

60. 'The Mo-S System (Molybdenum-Sulfur)', Bulletin of Alloy Phase Diagrams Vol. I No. 2 1980 95.

61. R.N. Bhattacharya, C.Y. Lee, Fred H. Pollak, D.M. Schleich, Optical study of amorphous MoS3: Determination of the fundamental energy gap, Journal of Non-Crystalline Solids, Volume 91, Issue 2, 1987, Pages 235-242, ISSN 0022-3093, https://doi.org/10.1016/S0022-3093(87)80306-X.

62. Fominski V, Demin M, Nevolin V, Fominski D, Romanov R, Gritskevich M, Smirnov N. Reactive Pulsed Laser Deposition of Clustered-Type MoSx (x ~ 2, 3, and 4) Films and Their Solid Lubricant Properties at Low Temperature. Nanomaterials. 2020; 10(4):653. https://doi.org/10.3390/nano10040653

63. *Chem. Mater.* 1993, 5, 6, 861–868 Publication Date:June 1, 1993 https://doi.org/10.1021/cm00030a024

64. L. Benoist, D. Gonbeau, G. Pfister-Guillouzo, E. Schmidt, G. Meunier, A. Levasseur, X-ray photoelectron spectroscopy characterization of amorphous molybdenum oxysulfide thin films, Thin Solid Films, Volume 258, Issues 1–2, 1995, Pages 110-114, ISSN 0040-6090, https://doi.org/10.1016/0040-6090(94)06383-4.

65. K. S. Liang, S. P. Cramer, D. C. Johnston, C. H. Chang, A. J. Jacobson, J. P. deNeufville and R. R. Chianelli, AMORPHOUS MoS3 AND WS3, Journal of Non-Crystalline Solids 42 (1980) 345-356

66. *Inorg. Chem.* 1984, 23, 9, 1215–1221 Publication Date:April 1, 1984 https://doi.org/10.1021/ic00177a010

67. Khudorozhko, G.F., Asanov, I.P., Mazalov, L.N. *et al.* X-ray photoelectron, emission, and absorption studies of the electronic structure of molybdenum and tungsten trisulfides and their intercalates. *J Struct Chem* **35,** 823–833 (1994). https://doi.org/10.1007/BF02578114

68. Cryst. Growth Des. 2020, 20, 7750−7760

69. Tang, M.L., Grauer, D.C., Lassalle-Kaiser, B., Yachandra, V.K., Amirav, L., Long, J.R., Yano, J. and Alivisatos, A.P. (2011), Structural and Electronic Study of an Amorphous MoS_3 Hydrogen-Generation Catalyst on a Quantum-Controlled Photosensitizer. Angew. Chem. Int. Ed., 50: 10203-10207. https://doi.org/10.1002/anie.201104412

70. K.S. Liang, J.P. deNaufville, A.J. Jacobson, R.R. Chianelli, F. Betts, Structure of amorphous transition metal sulfides, Journal of Non-Crystalline Solids, Volumes 35–36, Part 2, 1980, Pages 1249-1254, ISSN 0022-3093, https://doi.org/10.1016/0022-3093(80)90369-5.

71. A.M. Pastukhov, S.Yu. Skripchenko, Process for recovering molybdenum and tungsten from MoS3/WS3 precipitates, Hydrometallurgy, Volume 157, 2015, Pages 78-81, ISSN 0304-386X, https://doi.org/10.1016/j.hydromet.2015.08.001.

72. Energy Environ. Sci., 2013, 6, 2706

73. Escalera-López, D., Jensen, K. D., Rees, N. V., Escudero-Escribano, M., Electrochemically Decorated Iridium Electrodes with WS3−x Toward Improved Oxygen Evolution Electrocatalyst Stability in Acidic Electrolytes. Adv. Sustainable Syst. 2021, 5, 2000284. https://doi.org/10.1002/adsu.202000284

74. Mabayoje O, Liu Y, Wang M, Shoola A, Ebrahim AM, Frenkel AI, Mullins CB. Electrodeposition of MoS_x Hydrogen Evolution Catalysts from Sulfur-Rich Precursors. ACS Appl Mater Interfaces. 2019 Sep 11;11(36):32879-32886. doi: 10.1021/acsami.9b07277. Epub 2019 Aug 30. PMID: 31414789.

75. C.H. Chang, S.S. Chan, Infrared and Raman studies of amorphous MoS3 and poorly crystalline MoS2, Journal of Catalysis, Volume 72, Issue 1, 1981, Pages 139-148, ISSN 0021-9517, https://doi.org/10.1016/0021-9517(81)90085-3.

76. Lince, J.R., Pluntze, A.M., Jackson, S.A. *et al.* Tribochemistry of MoS_3 Nanoparticle Coatings. *Tribol Lett* 53, 543–554 (2014). https://doi.org/10.1007/s11249-014-0293-4

77. Edmond PAYEN, Slavik KASZTELAN, Jean GRIMBLOT, and Jean Pierre BONNELLE, "STUDY OF THE SULPHURIZATIDN OF WOS/ y-A120S CATALYSTS BY IN SITU LASER RAMAN SPECTROSCOPY" Catalysis Today, 4 (1988) 57-70 57 Elsevier Science Publishers B.V., Amsterdam-Printed in The Netherlands

78. C Sourisseau, O Gorochov, D.M Schleich, Comparative IR and Raman studies of various amorphous MoS3 and LixMoS3 phases, Materials Science and Engineering: B, Volume 3, Issues 1–2, 1989, Pages 113-117, ISSN 0921-5107, https://doi.org/10.1016/0921-5107(89)90188-8.

79. Zhipeng Huang, Chifang Wang, Lei Pan, Feng Tian, Xuanxiong Zhang, Chi Zhang, Enhanced photoelectrochemical hydrogen production using silicon nanowires@MoS3, Nano Energy, Volume 2, Issue 6, 2013, Pages 1337-1346, ISSN 2211-2855, https://doi.org/10.1016/j.nanoen.2013.06.016.

80. Vrubel, Heron & Merki, Daniel & Hu, Xile. (2012). Hydrogen evolution catalyzed by MoS3 and MoS2 particles. Energy Environ. Sci.. 5. 6136-6144. 10.1039/C2EE02835B.

81. Huanhui Chen, Guanxia Ke, Xiaochao Wu, Wanqing Li, Yongliang Li, Hongwei Mi, Lingna Sun, Qianling Zhang, Chuanxin He, Xiangzhong Ren, Amorphous MoS3 decoration on 2D functionalized MXene as a bifunctional electrode for stable and robust lithium storage, Chemical Engineering Journal, Volume 406, 2021, 126775, ISSN 1385-8947, https://doi.org/10.1016/j.cej.2020.126775.

82. Ye, H. L., Wang, L., Deng, S., Zeng, X. Q., Nie, K. Q., Duchesne, P. N., Wang, B., Liu, S., Zhou, J. H., Zhao, F. P., Han, N., Zhang, P., Zhong, J., Sun, X. H., Li, Y. Y., Li, Y. G., Lu, J., *Adv. Energy Mater.* 2017, 7, 1601602.

83. Ma, M., Zhang, S., Wang, L., Yao, Y., Shao, R., Shen, L., Yu, L., Dai, J., Jiang, Y., Cheng, X., Wu, Y., Wu, X., Yao, X., Zhang, Q., Yu, Y., Harnessing the Volume Expansion of MoS3 Anode by Structure Engineering to Achieve High Performance Beyond Lithium-Based Rechargeable Batteries. Adv. Mater. 2021, 33, 2106232. https://doi.org/10.1002/adma.202106232

84. Chang U, Lee JT, Yun JM, Lee B, Lee SW, Joh HI, Eom K, Fuller TF. In Situ Self-Formed Nanosheet MoS_3/Reduced Graphene Oxide Material Showing Superior Performance as a Lithium-Ion Battery Cathode. ACS Nano. 2019 Feb 26;13(2):1490-1498. doi: 10.1021/acsnano.8b07191. Epub 2018 Dec 27. PMID: 30580512.

85. Tsung-Wu Lin, Chia-Jui Liu, Jeng-Yu Lin, Facile synthesis of MoS3/carbon nanotube nanocomposite with high catalytic activity toward hydrogen evolution reaction, Applied Catalysis B: Environmental, Volumes 134–135, 2013, Pages 75-82, ISSN 0926-3373, https://doi.org/10.1016/j.apcatb.2013.01.004.

86. Scott, R.A., Jacobson, A.J., Chianelli, R.R., Pan, W.H., Stiefel, E.I., Hodgson, K.O., & Cramer, S.P. (1986). Reactions of MoS3, WS3, WSe3, and NbSe3 with lithium. Metal cluster rearrangement revealed by EXAFS. *Inorganic Chemistry, 25*, 1461-1466.

87. [Shim, Joongpyo, Kathryn A. Striebel, and Elton J. Cairns. "The Lithium/Sulfur Rechargeable Cell." Journal of The Electrochemical Society 149.10 (2002): A1321. Web.]

88. Zhang, Y., Mu, Z., Yang, C., Xu, Z., Zhang, S., Zhang, X., Li, Y., Lai, J., Sun, Z., Yang, Y., Chao, Y., Li, C., Ge, X., Yang, W., Guo, S., *Adv. Funct. Mater.* 2018, 28, 1707578. https://doi.org/10.1002/adfm.201707578

89. Zhu, X. Y., Zhao, W., Song, Y. Z., Li, Q. C., Ding, F., Sun, J. Y., Zhang, L., Liu, Z. F., *Adv. Energy Mater.* 2018, 8, 1800201. https://doi.org/10.1002/aenm.201800201

90. Qunchang Wang, Minghui Chen, Zhongmao Shan, Chengguo Sui, Lin Zhang, Shenglong Zhu, Fuhui Wang, Comparative study of mechanical and wear behavior of Cu/WS2 composites fabricated by spark plasma sintering and hot pressing, Journal of Materials Science & Technology, Volume 33, Issue 11, 2017, Pages 1416-1423, ISSN 1005-0302, https://doi.org/10.1016/j.jmst.2017.06.014.

91. Yang Sun, Jisi Wu, Lei Zhang, Fabrication of Ag-WS2 composites with preferentially oriented WS2 and its anisotropic tribology behavior, Materials Letters, Volume 260, 2020, 126975, ISSN 0167-577X, https://doi.org/10.1016/j.matlet.2019.126975.

92. Jin ZHOU, Chao MA, Xiao KANG, Lei ZHANG, Xin-li LIU, Effect of WS2 particle size on mechanical properties and tribological behaviors of Cu-WS2 composites sintered by SPS, Transactions of Nonferrous Metals Society of China, Volume 28, Issue 6, 2018, Pages 1176-1185, ISSN 1003-6326, https://doi.org/10.1016/S1003-6326(18)64755-7.

93. Rengifo, S., Zhang, C., Harimkar, S. *et al.* Effect of WS_2 Addition on Tribological Behavior of Aluminum at Room and Elevated Temperatures. *Tribol Lett* **65,** 76 (2017). https://doi-org.libproxy.library.unt.edu/10.1007/s11249-017-0856-2

94. Liu, H., Zhang, X., Li, S. *et al.* Synthesis and Thermoelectric Properties of SnSe by Mechanical Alloying and Spark Plasma Sintering Method. *J. Electron. Mater.* **46,** 2629–2633 (2017). https://doi.org/10.1007/s11664-016-4833-6

95. Chang, Y., Ruan, M., Li, F. *et al.* Synthesis process and thermoelectric properties of the layered crystal structure SnS_2. *J Mater Sci: Mater Electron* **31,** 5425–5433 (2020). https://doi-org.libproxy.library.unt.edu/10.1007/s10854-020-03105-3

96. Shouling Wang, Ronghua Wang, Lili Wang, Jie Chang, Fabrication and thermoelectric properties of bulk VSe2 with layered structure, Solid State Communications, Volume 318, 2020, 113983, ISSN 0038-1098, https://doi.org/10.1016/j.ssc.2020.113983.

97. Tokita M. Progress of Spark Plasma Sintering (SPS) Method, Systems, Ceramics Applications and Industrialization. Ceramics. 2021; 4(2):160-198. https://doi.org/10.3390/ceramics4020014

98. Tomonari Takeuchi et al 2008 J. Electrochem. Soc. 155 A679

99. Zheng, LJ., Zhang, BP., Han, CG. *et al.* Mechanical alloying-spark plasma sintering synthesis and thermoelectric properties of n-type $NiSe_{2+x}$ semiconductors: analysis of intrinsic defects and phase structures. *J Mater Sci: Mater Electron* **27,** 8363–8369 (2016). https://doi-org.libproxy.library.unt.edu/10.1007/s10854-016-4847-0

100. Molas, M.R., Nogajewski, K., Potemski, M. *et al.* Raman scattering excitation spectroscopy of monolayer WS_2 . *Sci Rep* **7,** 5036 (2017). https://doi.org/10.1038/s41598-017-05367-0

101. Germán Escalante, Roberto López, Francisco Noé Demesa, Gerardo Villa-Sánchez, Víctor Hugo Castrejón-Sánchez, and Israel Vivaldo de la Cruz , "Correlation between Raman spectra and color of tungsten trioxide (WO3) thermally evaporated from a tungsten filament", AIP Advances 11, 055103 (2021) https://doi.org/10.1063/5.0045190

102. Ho Suk Ryu, Zaiping Guo, Hyo Jun Ahn, Gyu Bong Cho, Huakun Liu. Investigation of discharge reaction mechanism of lithium|liquid electrolyte|sulfur battery, Journal of Power Sources, Volume 189, Issue 2, 2009, Pages 1179-1183, ISSN 0378-7753, https://doi.org/10.1016/j.jpowsour.2008.12.073.

103. M Rudolph *et al* 2022 *J. Phys. D: Appl. Phys.* **55** 015202

104. Nims, C., Cron, B., Wetherington, M. *et al.* Low frequency Raman Spectroscopy for micron-scale and *in vivo* characterization of elemental sulfur in microbial samples. *Sci Rep* **9,** 7971 (2019). https://doi.org/10.1038/s41598-019-44353-6

105. Mikhaylik, Yuriy & Akridge, James. (2004). Polysulfide Shuttle Study in the Li/S Battery System. Journal of The Electrochemical Society. 151. A1969-A1976. 10.1149/1.1806394.

106. Wu HL, Huff LA, Gewirth AA. In situ Raman spectroscopy of sulfur speciation in lithium-sulfur batteries. ACS Appl Mater Interfaces. 2015 Jan 28;7(3):1709-19. doi: 10.1021/am5072942. Epub 2015 Jan 14. PMID: 25543831.

107. Rosickyite (monoclinic gamma-sulphur) from La Presta Asphalt Mine, Neuchatel, Switzerland: new X-ray powder diffraction data DOI:10.5169/SEALS-60969

108. Jin-Tak Yeon *et al* 2012 *J. Electrochem. Soc.* **159** A1308 A. G. PINKUS, J. S. KIM, J. L. MCATEE, JR. C. B. CONCILIO, *On the Structure* of *Carbon Disuljide-Insoluble Sulfur,* JOURNAL OF POLYMER SCIENCE, VOL. XL, ISSUE 137 (1959)

109. Yu.L Mikhlin, A.V Kuklinskiy, N.I Pavlenko, V.A Varnek, I.P Asanov, A.V Okotrub, G.E Selyutin, L.A Solovyev, Spectroscopic and XRD studies of the air degradation of acid-reacted pyrrhotites, Geochimica et Cosmochimica Acta, Volume 66, Issue 23, 2002, Pages 4057-4067, ISSN 0016-7037, https://doi.org/10.1016/S0016-7037(02)00989-4.

110. Watanabe, Y (1974): The Crvstal Structure of Monoclinic 7-Sulphur. Acta Cryst., B30.1396-1401.

111. Arnold, C.L., Iheomamere, C.E., Dockins, M., Gellerup, S., Glavin, N.R., Muratore, C., Shepherd, N.D., & Voevodin, A.A. (2021). Composition, dielectric breakdown, and bandgap of ultra-thin amorphous boron oxynitride produced by magnetron sputtering. *Vacuum, 188*, 110211.